# UNIVERSIDAD DE GUANAJUATO
# CAMPUS LEÓN


## DIVISIÓN DE CIENCIAS E INGENIERÍAS

# The Dark Energy Spectroscopic Instrument: Simulations of the first year Lyman-$\alpha$ quasars observations

**Hiram Kalid Herrera Alcantar**

Proyecto de tesis como requisito parcial
para obtener el título profesional de
**Maestro en Física**

Asesora:
**Dra. Alma X. González-Morales**
División de Ciencias e Ingenierías
Universidad de Guanajuato

AGOSTO, 2020

*A mis padres,*
*Victoria y Javier,*
*con mucho amor*

# Abstract


## The Dark Energy Spectroscopic Instrument: Simulations of the first year Lyman-$\alpha$ quasars observations

The Baryon Acoustic Oscillations (BAO) provide a standard ruler to probe cosmology. In recent years there have been many projects dedicated to study BAO.

The first of the next generation of these projects will be the Dark Energy Spectroscopic Instrument (DESI), dedicated to the study of the effects of Dark Energy on the cosmic expansion history by studying BAO and Redshift Space Distortions.

DESI will measure the spectra of nearly 30 million galaxies distributed in a 14,000 $\deg^2$ area in a five-year period, including 0.7 million quasars at a redshift $z > 2.1$, that include a collection of absorption lines within their spectra, known as the Lyman-$\alpha$ forest.

This work develops a straight forward pipeline to simulate the observations of the Lyman-$\alpha$ quasars during the first year of DESI's operations. Including the simulation of the scheduling of the survey, the selection of mock targets that fulfill DESI's requirements, the assignment of the instrument fibers to observe these targets, the simulation of the Lyman-$\alpha$ quasar spectra and finally the measurement of the correlation function.

With this pipeline a realization of DESI's first year footprint was obtained, however the actual DESI footprint will depend on the weather presented during the year.

Concerning the simulation of the Lyman-$\alpha$ quasars spectra this work makes its strongest contribution to the DESI collaboration by providing a modification of the script dedicated to this task, `quickquasars`, this modification includes the feature to of simulating a given footprint with different quasar densities and with multiple exposure times.

With the modified version of `quickquasars`, two simulations of Lyman-$\alpha$ quasars were produced, one where all the quasars in the footprint have a single exposure, and another where there are multiple exposure times. The error bars of the correlation function of these realizations were compared obtaining a improvement of $\sim 20\%$ and $\sim 10\%$ in the auto-correlation and cross-correlation, respectively.

Keywords: **Cosmology** — **Lyman-Alpha Forest** — **Correlation Function** — **Simulations**.

# Contents

# List of Figures

# List of Tables

# General Introduction

The way the Universe is percieved has evolved a lot through the history of humanity. One of the first models of the Universe is the geocentric model made by the ancient Greece philosophers, which placed the Earth at the center of the Universe with all the stars an planets orbiting around it.

This theory prevailed until century XVI when Nicolaus Copernicus proposed the heliocentric model, which placed the sun at the center of the Universe. A few years later, Johannes Kepler proposed his laws on celestial motion based on the observations. Kepler's laws were the cornerstone for Newton's theory of universal gravitation, which described the movement of objects in the Universe due to an attractive "force" between two massive objects, called gravity.

Newton's theory remained valid for more than two-hundred years, until Albert Einstein proposed his theory of General Relativity, where gravity is not a force but a consequence of the curvature of space-time, this is the accepted description of gravity nowadays since it has been proven to be consistent with observations in small scales, for example the explanation of the perihelion precession of Mercury.

There are phenomena that give a hint of the existence of new physics that might implicate the modification of the theory of General Relativity, an example of these are the observations done by Edwin Hubble in 1929, which revealed that the Universe is expanding, then 70 years later the measurement of distant luminous objects called Type Ia Supernovas (SNIa) (Perlmutter et al., 1999; Riess et al., 1998), showed that the expansion is accelerated.

Einstein's theory does not predict the accelerated expansion of the Universe. A way to solve this problem, without questioning the validity of General Relativity, is to assume the existence of a "mysterious" component of the Universe that causes the accelerated expansion, this component is called *dark energy*.

The cosmological models can be constrained by measuring the distance between objects in space, but how are the distances in the Universe measured? One way is to use the luminosity of SNIa as *standard candles* based on a inverse square law. Another proposal is to use the Baryon Acoustic Oscillations (BAO) scale, to be described in section 1.2, as a *standard ruler* (Seo and Eisenstein, 2003).

On recent years there have been many projects dedicated to the study of BAO and its effects on the Universe's evolution, for example the Baryon Oscillation Spectroscopic Survey (Dawson, Schlegel, et al., 2013). The first of the next generation of these projects will be the Dark Energy Spectroscopic Instrument (DESI) a promising survey that will contain approximately 30 million of galaxies.

Within the galaxies that DESI will measure there are the Lyman-$\alpha$ quasars, which contain a set of absorption lines in their spectra known as the Lyman-$\alpha$ forest. BAO can be found in the correlation of forests of different quasars and its position can be used to trace the way the Universe has evolved through time.

The goal of this thesis is to describe the Lyman-$\alpha$ forest as a tool in the study of cosmic expansion, and forecast the Lyman-$\alpha$ quasars observations of DESI during its first year of operation. This thesis is structured as follows:

- Chapter 1 introduces some basic definitions in cosmology; some observables used to probe cosmology, such as the Cosmic Microwave Background and galaxy spectroscopic surveys and the phenomena that these surveys study, for example, BAO and the Redshift space distortions. Finally, the last section of this chapter introduces the Lyman-$\alpha$ forest and its relation with the study of cosmic expansion.
- Chapter 2 presents DESI, its design specifications, the type of galaxies to be observed and the main scientific goals of this collaboration.
- In chapter 3, the pipeline developed to simulate DESI's first year Lyman-$\alpha$ quasars observations, including the codes needed to achieve this task and the results obtained are discussed.
- Lastly, chapter 4 presents the conclusions of this work and future tasks.

# 1 The Lyman-$\alpha$ forest as a tool in cosmology

This chapter is dedicated to the introduction of some definitions to understand the Lyman-$\alpha$ forest and its importance to cosmology. To do so, basic cosmology concepts are introduced in section 1.1, then some techniques for probing and constraining cosmological models are described in section 1.2 and finally, the Lyman-$\alpha$ forest, the correlation function and its relation with the cosmic expansion history are presented in section 1.3.

This chapter is based on introductory cosmology books such as Liddle (2003); Ryden (2017) and S. Weinberg (2008), astrophysics books like Mo et al. (2010), the PhD thesis Bautista (2014) and references therein.

## 1.1 Cosmology Basics

Einstein's theory of relativity treats gravity as a consequence of the curvature of space-time due to matter and energy. This curvature is described by the *metric tensor* $g_{\mu\nu}$ related to the invariant line element

$$\mathrm{d}s^2 = g_{\mu\nu}\,\mathrm{d}x^\mu\,\mathrm{d}x^\nu\,, \tag{1.1}$$

where $\mu, \nu = 0$ correspond to temporal coordinates and $\mu, \nu = 1, 2, 3$ are spatial coordinates, for a flat space-time the metric is such that $g_{\mu\nu} = \mathrm{diag}(1, -1, -1, -1)$, this is called the *Minkowsky* metric.

The relation between the geometry of the space-time and the matter (energy) within it is given by the Einstein's field equations

$$G_{\mu\nu} = \frac{8\pi G}{c^4} T_{\mu\nu}, \tag{1.2}$$

where $G_{\mu\nu} = R_{\mu\nu} - \frac{1}{2}Rg_{\mu\nu}$ is the Einstein tensor, defined by the Ricci curvature tensor $R_{\mu\nu}$, the Ricci scalar or scalar curvature $R$ and the metric tensor, $T_{\mu\nu}$ is the energy-momentum tensor, related to the energy and momentum densities in the space-time, $G$ is the Newton's gravitational constant and $c$ is the speed of light in vacuum.

As mentioned before, the Universe is going through an accelerated expansion, Einstein's field equations do not predict this behavior, this issue is solved by adding a new term $T^{\mathrm{DE}}_{\mu\nu}$ to the right side of these equations associated with the existence of dark energy.

If dark energy is constant and homogeneously distributed through space, then eq. (1.2) can be rewritten in terms of a *cosmological constant*, associated with dark energy, such that

$$G_{\mu\nu} = \frac{8\pi G}{c^4}T_{\mu\nu} + \Lambda g_{\mu\nu}. \tag{1.3}$$

An important definition in cosmology is the *cosmological principle*, which states that *"The Universe is homogeneous and isotropic, at large scales"*. It is refered by large scales to distances at 100 Mpc* or larger.

A metric that describes an isotropic, homogeneous and expanding Universe is the *Friedmann-Lemaître-Robertson-Walker* (FLRW) metric,

$$ds^2 = c^2dt^2 - a^2(t)\left[\frac{dr^2}{1-kr^2} + r^2\left(d\theta^2 + \sin^2\theta d\phi^2\right)\right], \tag{1.4}$$

where $k$ is the curvature of the space and $a$ is the scale factor, which describes the expansion of the Universe.

There are three possible geometries of the Universe in this metric, if $k = 0$ it is flat and infinite; if $k > 0$ it is closed with spherical geometry and finite space; if $k < 0$ it is open with hyperbolic geometry and infinite space.

Considering a perfect fluid in thermodynamic equilibrium the energy-momentum tensor in the right hand of eq. (1.2), takes the simple form of

$$T_{\mu\nu} = \left(\rho + \frac{p}{c^2}\right)u_\mu u_\nu - pg_{\mu\nu}, \tag{1.5}$$

*A parsec (pc) is defined as the distance at which one astronomical unit subtends an angle of one arc second of parallax, this is $1\,\mathrm{pc} \approx 206{,}265\,\mathrm{au} \approx 3.086 \times 10^{16}\,\mathrm{m}$.

where $\rho$ and $p$ are the Universe's density and pressure, respectively, $u_\mu$ is the fluid's 4-velocity, that for the requirement of isotropy and homogeneity $u_0 = c$ and $u_i = 0$.

Using the FRLW metric and the energy-momentum tensor described above the following two equations can be derived from eq. (1.2), the first solving the temporal-temporal component and the second by taking the trace of the equation

$$\left(\frac{\dot{a}}{a}\right)^2 = \frac{8\pi G}{3}\rho - \frac{kc^2}{a^2} + \frac{\Lambda c^2}{3}, \tag{1.6}$$

$$\frac{\ddot{a}}{a} = -\frac{4\pi G}{3}\left(\rho + \frac{3p}{c^2}\right) + \frac{\Lambda c^2}{3}, \tag{1.7}$$

where the dots indicate a derivative with respect of time. The term $\dot{a}/a$ is often written as $H$ and it is called the *Hubble parameter*, usually expressed in units of $\mathrm{km\,s^{-1}\,Mpc^{-1}}$.

Combining eqs. (1.6) and (1.7) a third equation that describes the evolution of the Universe's density through time can be obtained,

$$\dot{\rho} + 3\frac{\dot{a}}{a}\left(\rho + \frac{p}{c^2}\right) = 0, \tag{1.8}$$

eqs. (1.6) to (1.8) are known as the *Friedmann Equations*.

It should be noted that there are three unknowns in the Friedmann equations $a, p$ and $\rho$, however there are only two independent equations, so there is a need for a third equation so that the system is solvable. This third equation is defined as the *equation of state* that relates the pressure with the density such that

$$p = \omega\rho c^2, \tag{1.9}$$

where $\omega$ is a dimensionless quantity related with the type of content in the Universe which the equations will be solved for, for example: for radiation and relativistic particles, $\omega = 1/3$; for non-relativistic matter like intergalactic dust and dark matter, $\omega = 0$; and for the cosmological constant $\omega = -1$.

For a flat Universe ($k = 0$) dominated by only one of the Universe content species,

the density equation has a solution,

$$\rho = \rho_0 a^{-3(\omega+1)}. \tag{1.10}$$

The equations can be rewritten in terms of the *critical density*, the density the Universe would have in a flat space at present days, defined by

$$\rho_c = \frac{3H_0^2}{8\pi G}, \tag{1.11}$$

where $H_0$ is the expansion rate today, parameterized as

$$H_0 = 100\, h\, \mathrm{km\, s^{-1}\, Mpc^{-1}}, \tag{1.12}$$

$h$ is known as the *dimensionless Hubble parameter*.

The critical density is used to define the *density parameter* $\Omega_i = \rho_i/\rho_c$ of each content species. Also, the curvature density parameter can be defined as $\Omega_k = -k^2c^2/H_0^2$ and the cosmological constant density parameter as $\Omega_\Lambda = \Lambda c^2/H_0^2$. These density parameters follow the relation

$$\Omega_0 = \Omega_m + \Omega_r + \Omega_\Lambda = 1 - \Omega_k, \tag{1.13}$$

where $m$ and $r$ denote matter and radiation respectively. So eq. (1.6) can be written simply as

$$H = H_0\left[\Omega_m a^{-3} + \Omega_r a^{-4} + \Omega_\Lambda + \Omega_k a^{-2}\right]^{1/2}. \tag{1.14}$$

Most of the objects in the Universe, like galaxies and stars have a set of emission (or absorption) lines within its spectrum, these lines have a defined wavelength in the rest frame, but when the spectrum is observed by the telescopes on Earth, these lines appear shifted to the red of the spectrum, this is the definition of *redshift*, a generalization of the Doppler effect for electromagnetic waves.

Mathematically the redshift is defined as

$$z = \frac{\lambda_{\mathrm{obs}}}{\lambda_{\mathrm{em}}} - 1, \tag{1.15}$$

where $\lambda_{\mathrm{obs}}$ and $\lambda_{\mathrm{em}}$ are the wavelengths on the observation and the emitted points,

respectively.

The redshift can also be defined in terms of the scale factor as

$$a = \frac{1}{z+1}, \tag{1.16}$$

with this definition eq. (1.14) is written in terms of the redshift as

$$H(z) = H_0\left[\Omega_m(1+z)^3 + \Omega_r(1+z)^4 + \Omega_\Lambda + \Omega_k(1+z)^2\right]^{1/2}. \tag{1.17}$$

The observations made by Planck Collaboration et al. (2018) lead to $\Omega_m = 0.315 \pm 0.007$, $\Omega_\Lambda = 0.685 \pm 0.007$ and $\Omega_k = 0.001 \pm 0.002$ and $H_0 = 67.4 \pm 0.5\ \mathrm{km\,s^{-1}\,Mpc^{-1}}$, this leads to a value of $\Omega_r \sim 10^{-4}$. Since the radiation and curvature terms are small compared to the matter and cosmological constant densities they will be neglected from now on.

Now, the concept of distances in the Universe can be defined, this is an important definition since an observable quantity, for example its redshift or luminosity, can be connected with the distance at which this object is from the observer and use this distance to constrain a cosmological model.

To understand the distances in the Universe, the concept of *co-moving coordinates* is needed. Since the Universe is expanding, it is convenient to describe the positions of objects in the Universe in terms of the scale factor by the following equation

$$\mathbf{r}(t) = a(t)\mathbf{x}, \tag{1.18}$$

where $\mathbf{r}(t)$ and $\mathbf{x}$ are the *physical* and *co-moving* distances between two points. The co-moving distance is set at a given time $t_0$ and remains constant as the Universe expands, while the physical distance can be found at any time $t$ trough the scale factor.

The co-moving distance of an object of redshift $z$ relative to the Earth can be computed by the relation

$$\chi(z) = c\int_0^z \frac{dz'}{H(z')}. \tag{1.19}$$

Another concept is the *angular diameter distance* $D_A$, the distance at which an

object of size $l$ would have an apparent angular size $\theta$ in the sky, it is defined in terms of the co-moving distance as

$$D_A(z) = \frac{c}{H_0\sqrt{|\Omega_k|}(1+z)} \sin\left(\frac{\sqrt{\Omega_k}H_0}{c}\chi(z)\right), \tag{1.20}$$

in the limit where $\Omega_k = 0$, it simply becomes $D_A(z) = \chi(z)/1 + z$.

The distance the light from a source of luminosity $L$ would have to travel to have the flux observed $F_{\text{obs}}$ in Earth is defined as the *luminous distance* $D_L$, this distance is such that

$$D_L = \sqrt{\frac{L}{4\pi F_{\text{obs}}}}, \tag{1.21}$$

it is related to the angular diameter distance by

$$D_L(z) = (1+z)^2 D_A(z). \tag{1.22}$$

The last distance to be defined in this section will be the *Hubble distance*, the Universe length scale at a given redshift $z$, mathematically

$$D_H(z) = \frac{c}{H(z)}. \tag{1.23}$$

## 1.2 Probing cosmology

The most accepted model to describe the Universe is the $\Lambda CDM$ model, which assumes that the Universe is composed primarily by three components; non relativistic (cold) dark matter, baryons, and dark energy. This model predicts the formation of structures in the Universe and the observed accelerated expansion. The model has a set of six free parameters, from which more quantities can be calculated. In this subsection three observables will be mentioned: the Cosmic Microwave Background, the Baryon Acoustic Oscillations and the Redshift-Space distortions, that can be used to constrain some (if not all) of the cosmological parameters.

### 1.2.1 Cosmic Microwave Background

During its early stages the Universe was a hot, dense plasma of photons and baryons. During this epoch the photons were energetic enough to keep protons and electrons from binding and therefore, neutral atoms were not able to exist.

When the Universe expanded and cooled enough the energy of photons was lower than the ionizing energy of neutral Hydrogen, then the protons and electrons formed the first neutral atoms, starting an epoch known as *recombination*.

A time shortly after this, photons decoupled from matter starting to travel through the Universe without being scattered, this stage is known as *decoupling*. The photons released during decoupling are refered as the *Cosmic Microwave Background* (CMB) radiation, and it can be detected at present days in all directions.

The existence of the CMB was predicted in 1948 (Alpher and Herman, 1949), this prediction was confirmed after its detection in 1965 (Penzias and Wilson, 1965) during the testing of a radio receiver built for radio astronomy in Bell Labs in New Jersey. Later observations of the CMB made by the COBE satellite (Smoot, 1999), revealed that the CMB follows a black body spectrum with a temperature of 2.73 K with 0.14% precision, also revealing anisotropies in its thermal spectrum of the order of $10^{-5}$, confirming predictions made in 1970 (Peebles and Yu, 1970). The observations made by COBE were corroborated by WMAP (Bennett et al., 2013) with 0.02% precision on the spectrum temperature of the CMB and at least $\sim 15\%$ on the cosmological parameters.

The latest results on the studies of the CMB were made by the Planck satellite (Planck Collaboration et al., 2018), constraining the $\Lambda CDM$ model with measurements of at least $\sim 13\%$ precision, as an example the measurement of the parameter $\Omega_b h^2$ of Planck improves that of WMAP by a factor of $\sim 2$.

### 1.2.2 Galaxy Spectroscopic Surveys

Another way of probing cosmological models is through the analysis of a galaxy spectroscopic survey that contains the information of the spectra of as many galaxies as possible. This is usually done in three stages: the selection of the area to be surveyed, the selection of the targets of interest to be studied, and finally the measurement of the targets spectra to obtain their redshift.

The first ever spectroscopic survey done by the Center of Astrophysics (CfA; Davis et al., 1982) measured the spectra of around 2,000 galaxies between 1977 and 1982, this was later extended to nearly 15,000 galaxies with CfA2 (Geller and Huchra, 1989) during the first years of the 90s.

The number of galaxies in a survey has increased exponentially over the pass of the years. The Two-degree-Field Galaxy Redshift Survey (2dFGRS; Colless et al., 2001) collected around 250,000 galaxy spectra from 1997 to 2002, next the Sloan Digital Sky Survey (SDSS) during a 4 stages project (Blanton et al., 2017; Eisenstein, D. H. Weinberg, et al., 2011; York et al., 2000) collected altogether the spectra of nearly 4 million galaxies from 2003 until 2020, the vast majority ($\sim$ 3 million) from the BOSS (Dawson, Schlegel, et al., 2013) and eBOSS (Dawson, Kneib, et al., 2016) projects.

The next big jump in a galaxy survey will be done by the Dark Energy Spectroscopic Instrument (DESI), described in chapter 2, the first of the new generation spectroscopic surveys that will collect the spectra of 30 million targets from 2020 to 2025. Other new generation surveys are Euclid (Laureijs et al., 2011) and Roman, formerly known as WFIRST (Spergel et al., 2015), a pair of space telescopes that are expected to be launched in 2022 and 2025, respectively.

Once the data of galaxy survey is available, processes like the galaxies' evolution, the large scale structure formation in the Universe can be studied and even the constrain the cosmological models is possible through the study of different phenomena like the Baryon Acoustic Oscillations and the Redshift Space distortions, to be briefly described next.

### Baryon Acoustic Oscillations

Before recombination, within the hot plasma in the Universe there were some regions with overdensities, which attracted more matter to its center due to the effects of Gravity, at the same time the radiation pressure exerted a force pulling matter away from them, oscillating and creating relativistic sound waves propagating through the plasma.

A brief period after recombination, in an epoch defined as the *drag epoch* at a redshift $z_d$, baryons stop being affected by radiation pressure, freezing the sound waves and leaving a shell of baryonic matter around each overdensity. The process is known as the *Baryon Acoustic Oscillations* (BAO).

BAO leaves an imprint on the clustering of galaxies and matter, generating a small excess on the number of galaxies in the shell radius at the drag epoch $r_d$. This radius is only affected by the expansion of the Universe, in the sense that in co-moving coordinates $r_d$ remains constant and its size at another time $t$ is found by the scale factor (see eq. (1.18)), therefore it provides a standard ruler for measuring the expansion history of the Universe.

The radius of BAO in co-moving coordinates can be measured through the anisotropies of the CMB. The latest results of Planck (Planck Collaboration et al., 2018) provide a 0.05% precision measurement of the angular acoustic scale; this along with the 0.7% precision constrains on $\Omega_m h^2$, $h$ and $\Omega_b h^2$ lead to a 0.2% precision BAO scale value of $r_d = 147.2\,\mathrm{Mpc}$.

The BAO imprint on galaxies clustering was first detected in 2005 by studying the correlation function of Luminous Red Galaxies in a redshift range $0.16 < z < 0.47$ (Eisenstein, Zehavi, et al., 2005).

Measurements of the BAO scale for redshifts $z > 2$, can be done through the Lyman-$\alpha$ forest, to be defined in section 1.3, the latest results on the study of BAO through the Lyman-$\alpha$ forest auto-correlation and cross-correlation, defined in section 1.3.2, provide a measurement of the Hubble distance at an effective redshift $z = 2.34$ with 3.3% and 4.9% precision, respectively (Blomqvist et al., 2019; de Sainte Agathe et al., 2019).

### Redshift Space Distortions

The redshift of a galaxy is composed by two contributions: the redshift due to the expansion of the Universe related to the Hubble constant and the distance to the object by $z = H_0 d$, and the redshift due to the peculiar velocity at which it is receding from us related to the redshift by $z = v/c$.

The peculiar velocity causes a distortion on the spatial distribution of the galaxies when plotted as a function of the redshift; this is effect is known as the *Redshift Space distortions* (RSD) and can come in two possible ways depending on the distortion along the line of sight of the observer: elongated, known as the *Fingers of God* effect; or flattened, known as the *Kaiser* effect.

RSDs are related to the clustering of matter and their measurement can be used to

test General Relativity, probe cosmology and the growth of structure through the parameter $f\sigma_8$.

## 1.3 The Lyman-$\alpha$ forest

Quasars or quasi-stellar objects (QSOs*) are particular type of galaxies, that contain an extremely luminous active nucleus surrounded by an accretion disk filled with gas. As material falls into the nucleus, an enormous amount of energy is emitted as electromagnetic radiation that can be detected from very far distances of the Universe. The high energy of the nucleus is such that it outshines the rest of the components of the galaxy, and it creates the emission lines that characterize QSOs; for example, the emission lines corresponding to Hydrogen transitions like Lyman-$\alpha$ and Lyman-$\beta$, and those corresponding to metals such as two-times and three-times ionized Carbon [CIII] and [CIV], ionized Magnesium [MgII], two-times ionized Oxygen [OII], just to mention some.

If quasars at $z > 2$ are observed with an optical telescope, there will be found a collection of absorption lines (see fig. 1.1) blue-wards the main Lyman-$\alpha$ emission line located at $\lambda_{\mathrm{Ly}\alpha} = 1216\,\text{Å}$ in the rest frame. These lines are caused mainly due to the interaction of the quasar light with the neutral hydrogen in the intergalactic medium (IGM) located within the light of sight between the observer and the quasar.

### 1.3.1 The Gunn-Peterson Effect

The physical process behind the Lyman-$\alpha$ forest is the Gunn-Peterson effect (Gunn and Peterson, 1965). This effect takes into account that the Lyman-$\alpha$ cross section is very large, so photons coming from a distant quasar reaching the Lyman-$\alpha$ wavelength after being redshifted, will be absorbed and re-emitted. Therefore, if there is a considerable amount of hydrogen within the trajectory of the quasar light, an absorption line will be observed in the spectrum.

The amplitude of the absorption lines in the Lyman-$\alpha$ forest is related directly to the optical depth $\tau(\lambda)$, defined as the measure of the absorption of a medium of specific depth that the photons go through, in this case HI columns. This can be quantified

*For the extension of this thesis QSO and quasar will be used indistinctly.

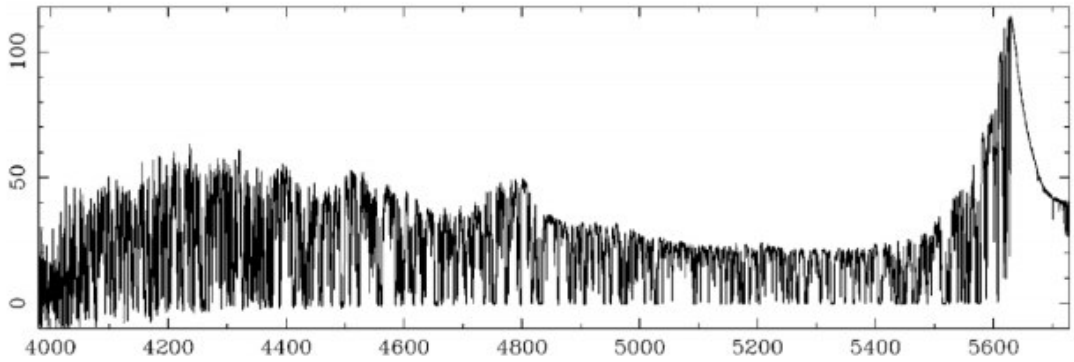


**Figure 1.1:** Example of a quasar spectrum containing the Lyman-$\alpha$ forest. This spectrum corresponds to the QSO1422+23 (V=16.5) quasar, located a redshift $z = 3.62$. The spectrum was originally obtained by the Kick High Resolution Spectrograph.The Lyman-$\alpha$ Forest is found blue-wards the Lyman-$\alpha$ peak located at $\sim 5600\,\text{Å}$. Figure taken from Bautista (2014).

by the transmitted flux $F(\lambda)$ in the forest,

$$F(\lambda) = e^{-\tau(\lambda)}. \tag{1.24}$$

Mathematically, the optical depth of a HI cloud located at a redshift $z$, with a local number density $n_{\text{HI}}(z)$ and an excitation cross-section $\sigma(\nu)$ for HI in a given frequency $\nu$ is given by

$$\tau = \int \sigma(\nu) n_{\text{HI}}(z) \frac{c}{H(z)} \frac{\mathrm{d}\nu}{\nu}, \tag{1.25}$$

For a Lyman-$\alpha$ photon, the cross section is given by

$$\sigma(\nu) = \frac{\pi e^2}{m_e c} f \delta_D(\nu - \nu_\alpha), \tag{1.26}$$

where $f = 0.416$ is the oscillator strength and $\nu_\alpha = 2.466 \times 10^{15}\,\text{Hz}$ is the frequency of the Lyman-$\alpha$ photon, $e$ is the electron charge, $m_e$ is the electron mass*.

*For this section Gaussian units will be used, as it is common in astronomy:
$e = 4.803 \times 10^{-10}\,\text{statC}$
$m_e = 9.191 \times 10^{-28}\,\text{g}$,
$c = 2.997 \times 10^{10}\,\text{cm}\,\text{s}^{-1}$.

Combining eqs. (1.25) and (1.26), the optical depth is

$$\tau = \sigma_\alpha n_{\rm HI}(z)\frac{c}{H(z)} = 4.446 \times 10^{-18}\,{\rm n_{HI}}(z)\frac{c}{H(z)}, \tag{1.27}$$

where the cross-section $\sigma_\alpha$ of HI for a Lyman-$\alpha$ photon has been defined as $\sigma_\alpha = \pi e^2 f/\nu_\alpha m_e c = 4.446 \times 10^{-18}\,{\rm cm}^2$.

The HI number density $n_{\rm HI}(z)$ is given by

$$n_{\rm HI}(z) = \frac{\rho_c}{m_p} X \Omega_b (1+z)^3 = 2.515 \times 10^{-7}\,{\rm X}\left(\frac{\Omega_b h^2}{0.0224}\right)(1+z)^3 {\rm cm}^{-3}, \tag{1.28}$$

where $m_p$ is the mass of the proton, $X$ is the fraction of neutral hydrogen in the Universe and $\Omega_b$ is the baryon density parameter (Mo et al., 2010).

The observed spectra of quasars at redshifts $z > 6$ show a suppression of the flux, this is called the *Gunn-Peterson trough* and is a proof that the Universe went through a process on which it when from being neutral after recombination to be mostly ionized, this epoch; is called *reionization*.

The optical depth can be also expressed as

$$\tau(\nu) = \Sigma(\nu) N_{\rm HI}(z), \tag{1.29}$$

where $\Sigma(\nu)$ is the cross section integrated over the line of sight and $N_{\rm HI}(z)$ is the neutral hydrogen column density, it is observed that the Lyman-$\alpha$ forest is caused by columns densities in the range of $10^{12}$ and $10^{17}{\rm cm}^{-2}$.

For a system with a column density $N_{\rm HI}(z) > 10^{17}{\rm cm}^{-2}$ light with a wavelength lower than the Lyman limit ($\lambda = 912\,$Å in rest frame) might be completely absorbed, hence break in the spectrum may be found, these systems are often referred as *Lyman Limit Systems* (LLS).

There are systems which column density is $N_{\rm HI}(z) > 10^{20}{\rm cm}^{-2}$, this density is enough to produce a large gap in the spectrum, such systems are referred as *Damped Lyman Alpha* (DLA) systems.

There are some quasars that present a small break just after an emission line, this is due to gas flowing from the accretion disk in the observer's direction; these systems are known as *Broad Absorption Line* (BAL) systems. Although these absorptions

are not due to neutral hydrogen, it is important to define these systems.

Within the quasars spectra there are another features that can be mixed with the Lyman-$\alpha$ forest, for example the absorption lines due to metals (Blomqvist et al., 2019; de Sainte Agathe et al., 2019) and the effects of the Ultraviolet Background Fluctuations (Gontcho A Gontcho et al., 2014), even though these effects will not be described in this thesis they are important for the analysis of the Lyman-$\alpha$ forest.

### 1.3.2 Tracing the Universe expansion history

Although the forest contains information about dark matter and the cosmic expansion history, the latter will be the focus of this thesis. A way the information about the cosmic expasion can be extracted from the Lyman-$\alpha$ forest is through the *three-dimensional correlation function*, related entirely to the absorption lines within quasar spectra.

To construct the correlation function, the transmitted flux $F(\lambda)$ can be rewritten in terms of the ratio of the observed flux $f(\lambda)$ and the un-absorbed flux $C(\lambda)$ of the quasar, this is also known as the *continuum*, then the transmission fluctuations are defined as

$$\delta_F(\lambda) = \frac{F(\lambda)}{\bar{F}(z)} - 1 = \frac{f(\lambda)}{C(\lambda)\bar{F}(z)} - 1, \tag{1.30}$$

where $\bar{F}(z)$ is the mean transmitted flux at a given redshift, assumed to be the same for all quasars. The continuum is fitted for each quasar using one of different techniques (see section 6.1 of Bautista (2014)).

Once the fluctuations are computed for all the quasars in a sample, the correlation function can be constructed, either by using the Lyman-$\alpha$ forest auto-correlation or Lyman-$\alpha$ forest-Quasar cross-correlation estimators defined, respectively, by

$$\hat{\xi}(A) = \frac{\sum_{i,j\in A} \omega_i \omega_j \delta_i \delta_j}{\sum_{i,j\in A} \omega_i \omega_j}, \tag{1.31}$$

$$\hat{\xi}(A) = \frac{\sum_{i,k\in A} \omega_i \delta_i}{\sum_{i,k\in A} \omega_i}, \tag{1.32}$$

where $A$ is a bin of a grid of distances between two redshift slices, $i$ and $j$ (auto-

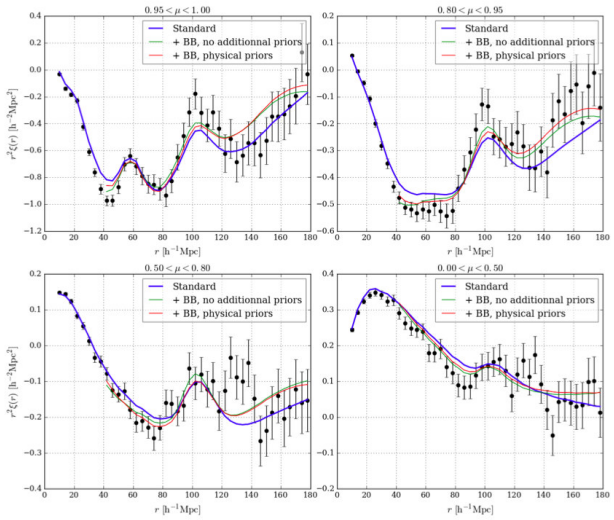


**Figure 1.2:** Measurement of the Lyman-$\alpha$ forest auto-correlation function split in four ranges of four ranges of $\mu = r_\parallel / r$. Figure taken from de Sainte Agathe et al. (2019).

correlation), or a redshift slice $i$ and a quasar $k$ (cross-correlation) within the spectra and $\omega_i$ is the weight of the $i$-th redshift slice, constructed in terms of the inverse variance of the transmission fluctuations $\delta_i$, refer to section 6.2.1 of Bautista (2014) or section 3.2 in de Sainte Agathe et al. (2019) for a more detailed description.

The distances can be computed converting the value of the redshift bin and the quasar angular positions ($RA$, $DEC$) into co-moving positions using a fiducial cosmology to compute their co-moving distances $\chi(z)$ by eq. (1.19), such that

$$\mathbf{x} = [\chi(z)\cos(DEC)\sin(RA), \chi(z)\cos(DEC)\cos(RA), \chi(z)\sin(DEC)]. \quad (1.33)$$

A vector, $\mathbf{r} = \mathbf{x}_i - \mathbf{x}_j$, can be traced between two redshift slices that can be split into two components $r_\parallel$ and $r_\perp$. Usually the grid of distances is such that the parallel component is $0 < r_\parallel < 200\,h^{-1}\,\mathrm{Mpc}$ for the auto-correlation and $-200 < r_\parallel < 200\,h^{-1}\,\mathrm{Mpc}$ for the cross-correlation, the perpendicular component is $0 < r_\perp < 200\,h^{-1}\,\mathrm{Mpc}$ for both correlations. These distances are split into bins of $4\,h^{-1}\,\mathrm{Mpc}$. For a given bin in $A$, two elements whose distance components fall into this bin are chosen. The auto-correlation of those redshift slices that are in the same line of sight and the cross-correlation of a quasar with its own forest are ignored.

An example of the measurement of the Lyman-$\alpha$ forest auto-correlation can be seen

in fig. 1.2, a peak can be seen in all four subfigures at $\sim 100\,h^{-1}$ Mpc this corresponds to the BAO scale, in the top left panel a second peak at $\sim 60\,h^{-1}$ Mpc is seen, this is an example of contamination due to the presence metals in quasar spectra.

The position of the BAO scale peak is usually described in terms of two parameters, $\alpha_\parallel$ and $\alpha_\perp$, that adjust the position of the peak relative to the predicted by a fiducial cosmology. These parameters are related to the Hubble distance and the angular diameter distance by

$$\begin{aligned} \alpha_\parallel &= \frac{D_H(\bar{z})/r_d}{[D_H(\bar{z})/r_d]_{\text{fid}}}, \\ \alpha_\perp &= \frac{D_A(\bar{z})/r_d}{[D_A(\bar{z})/r_d]_{\text{fid}}} \end{aligned} \tag{1.34}$$

where $\bar{z}$ is an effective redshift. From eq. (1.23) it follows that the Hubble parameter in terms of $\alpha_\parallel$ is given by

$$H(\bar{z})r_d = \frac{c}{\alpha_\parallel [D_H(\bar{z})/r_d]_{\text{fid}}}, \tag{1.35}$$

this way the cosmic expansion history can be studied through the Lyman-α forest at different effective redshifts.

During this chapter, the importance of BAO as a cosmic expansion tracer has been discussed. As mentioned before, the Lyman-α forest provides an important tool to study BAO through a galaxy spectroscopic survey. Modern cosmology demands the increment on the measurements precision, on galaxy surveys this precision is directly related with the sample size, therefore it arises the need of larger surveys, in this sense DESI has been mentioned as the first of the next generation of galaxy spectroscopic surveys. This motivates the discussion of the details of DESI and its scientific goals during the next chapter.

# 2 The Dark Energy Spectroscopic Instrument

The goal of this chapter is to introduce the Dark Energy Spectroscopic Instrument (DESI). A description of the instrument design, target selection strategy and DESI's scientific goals will be given. This chapter is based mainly on DESI Collaboration et al. (2016a); DESI Collaboration et al. (2016b); Dey et al. (2019); Martini et al. (2018) and the DESI Legacy Imaging Surveys public website*.

## 2.1 The Instrument

DESI is composed by the Mayall 4-meter telescope, an optic corrector, a focal plane system, the fibers themselves, and 10 identical spectrographs. In this section, some information about these components is given. A more detailed description can be found in DESI Collaboration et al. (2016b) and Martini et al. (2018).

### The Mayall Telescope

The first component is the telescope itself. DESI is mounted in the 4-meter Mayall Telescope located in the Kitt Peak National Observatory in Arizona. Mayall is a reflector telescope, installed on an equatorial mount.

In February 2018 Mayall stopped working to begin with an intensive redesign for the installation of DESI. This redesign includes an update in the telescopic control system and a replacement of the cage and ring siting on the top of the telescope. Figure 2.1 shows the interior of the Mayall telescope.

*http://legacysurvey.org

**Figure 2.1:** Interior of the Mayall 4-m telescope located in the Kitt Peak National Observatory in Arizona. Figure taken from the DESI collaboration public web page: https://www.desi.lbl.gov.

## Corrector

The design of DESI includes a prime focus corrector composed of four fused silica lenses, from which two are aspheric. It also includes an Atmospheric Dispersion Compensator (ADC) that includes two borosilicate lenses, this compensator serves to meet DESI's blur requirements at off-zenith angles.

The corrector is designed to operate on the wavelengths $360 - 980\,\mathrm{nm}$, at zenith angles up to 60°. The design of this corrector allows the 5000 fibers from DESI to be arranged in an $8\,\mathrm{deg}^2$ area. Figure 2.2 shows the optical design of the corrector, for more details about this component refer to section 3 of DESI Collaboration et al. (2016b).

## Focal plane system

DESI's focal plane system is composed by 5000 robotic fiber positioners, each of these positioners aims a fiber to a unique target in each observation. The focal plane system is divided into 10 petals of 36° that contain 500 fiber positioners each (see fig. 2.3).

Additionally, each petal contains a Guide, Focus and Alignment (GFA) sensors that focus the focal plane; and 12 field fiducials, light point sources that serves as a reference for the camera. The fiber positioners are controlled by a fiber assignment and an anti-collision software to prevent problems while positioning the fibers to a target during observations.

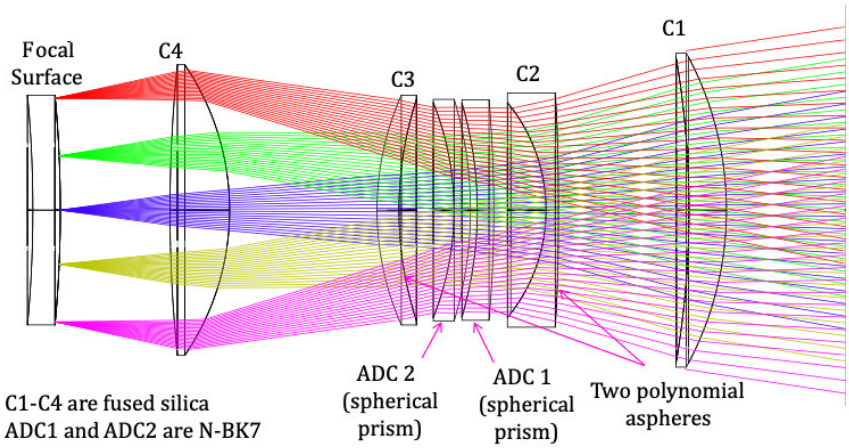


**Figure 2.2:** Corrector optical design. It contains four fused silica lenses, from which two are aspheric, along with an Atmospheric Dispersion Compensator (ADC) that incluides two borosilicate lenses. Figure taken from DESI Collaboration et al. (2016b).

## Fiber System

Each of the positioners from the Focal Plane System are connected to the spectrographs by 49.5 m long optical fibers to transmit the light of the 5,000 targets observed. Each of these fibers have a 107 µm diameter. And are divided in ten groups of 500 fibers connected to a single spectrograph.

## Spectrographs

DESI has ten identical spectrographs that work on three wavelength channels: blue ($360-593$ nm), red ($566-772$ nm) and near-infrared ($747-980$ nm) with a resolving power of $2000-3200$, $3200-4100$ and $4100-5000$, respectively; this is obtained by dividing the wavelength $\lambda$ by the smallest difference in the wavelength the band can distinguish $\Delta\lambda$.

Each of the spectrographs are connected to a group of 500 fibers of the Fiber System. Figure 2.4 shows one of DESI's spectrographs.

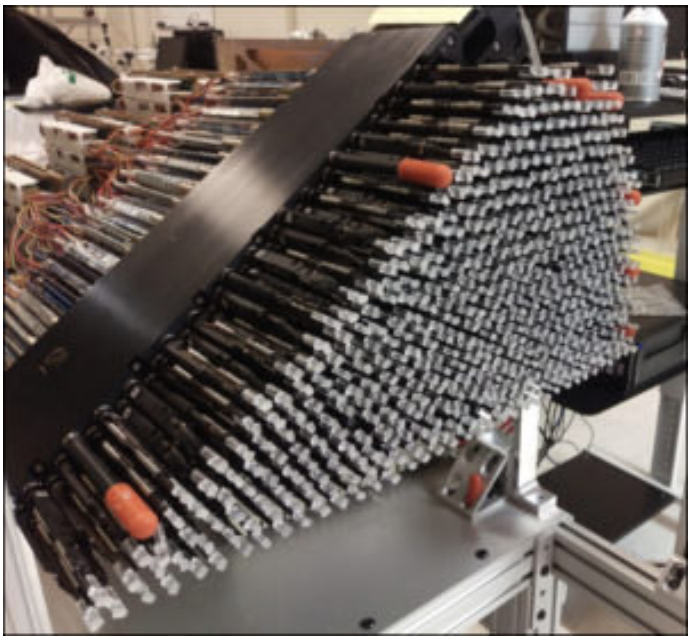

**Figure 2.3:** One of the 10 petals of DESI's Focal Plane System (FPS), it contains 500 fiber positioners, 12 light point sources as a reference for the camera and a Guide, Focus and Alignment sensor to focus the focal plane. Figure taken from DESI's public web page: https://www.desi.lbl.gov.

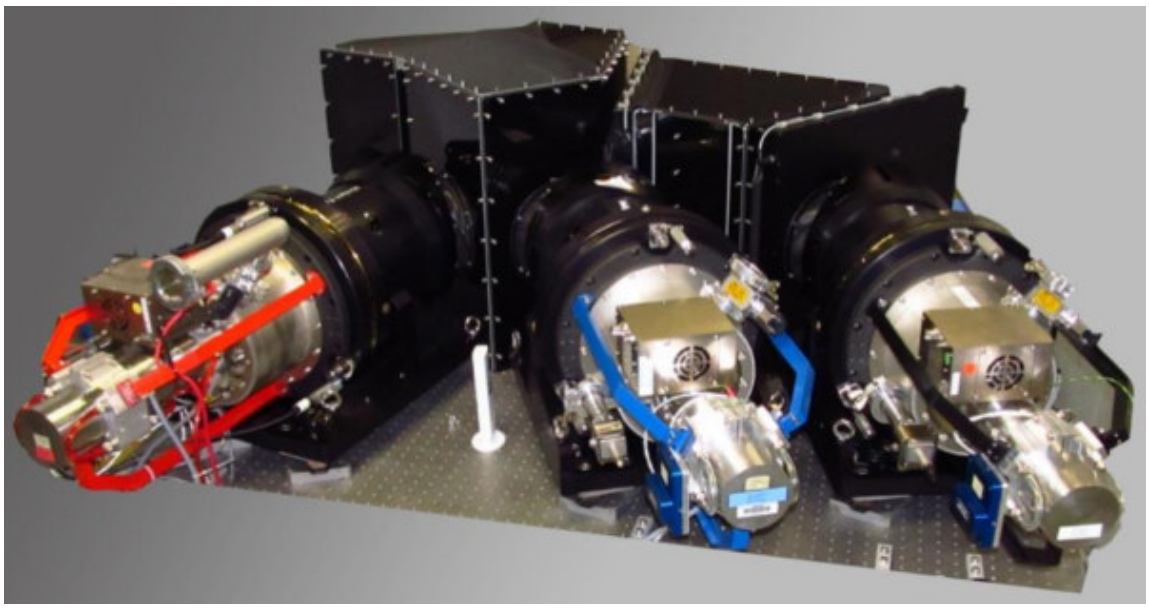

**Figure 2.4:** One of the ten spectrographs of DESI. Each spectrograph has three wavelength bands blue, red and near-infrared. Figure taken from DESI's public web page: https://www.desi.lbl.gov.

## 2.2 Targets

To achieve its scientific goals, DESI will obtain spectra from approximately 30 million of extra-galactic sources, divided into four classes: the Bright Galaxies, Luminous Red Galaxies, Emission Line Galaxies and quasars. This section is dedicated to discussing the characteristics of the survey of each of these objects, such as sample size, redshift range and redshift measurement strategy.

### 2.2.1 Bright Time Targets

These are the brightest targets within DESI's survey and will be observed during the *Bright Time* program, the time when moonlight can affect the quality of the observations on fainter objects.

#### Bright Galaxies

The Bright Galaxy Sample (BGS) is expected to reach 9.8 million targets, within a redshift range of $0.05 < z < 0.4$ and will be covered using DESI's spectrograph *r-band* up to a magnitude 19.5 limit.

### 2.2.2 Dark Time Targets

The *Dark Time* program includes the 21 darkest nights of the month, lacking of moonlight, and having optimal observation conditions. DESI will observe the following targets:

#### Luminous Red Galaxies

The Luminous Red Galaxies (LRGs) are quite massive, most of its content are old stars, this produces their characteristic red color (in rest-frame). The sample size of these objects is expected to be 4 million.

LRGs will be selected in a redshift range $0.4 < z < 1$, the lowest redshift in the *Dark Time* program. The redshift of those LRGs below $z < 0.6$ will be estimated using previous surveys photometry (Eisenstein, Annis, et al., 2001; Padmanabhan et al., 2007). For those with $z > 0.6$, the redshift will be estimated through the "1.6 µm bump", a maximum in the spectral energy distribution around 1.6 µm in rest frame

(see fig. 2.5), for further details refer to section 3.2 on DESI Collaboration et al. (2016a).

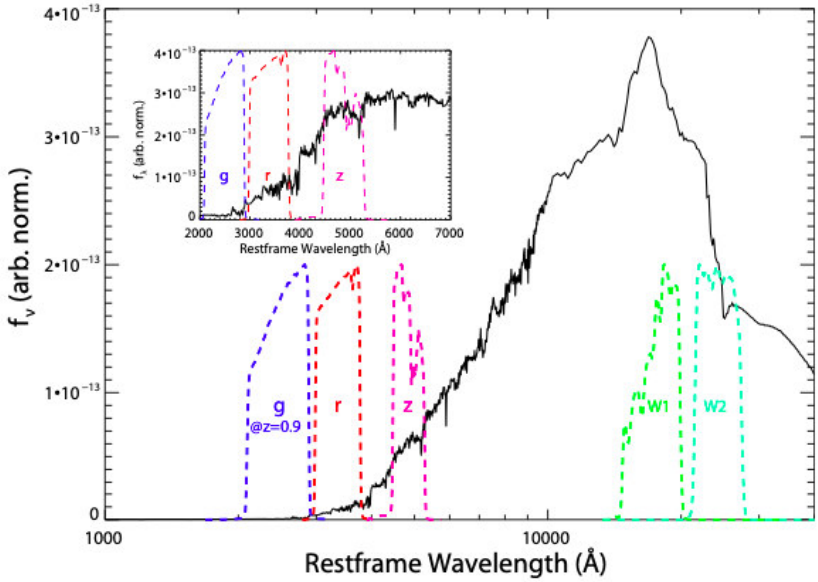


**Figure 2.5:** Example of a Luminous Red Galaxy (LRG) rest frame spectra. The flux shows a maximum at the spectrum around 16,000 Å, this is the so called "1.6 µm bump". The inset shows a close up to a break in the spectrum around 4000 Å, this is another characteristic of LRG's spectra. Figure taken from DESI Collaboration et al. (2016a).

### Emission Line Galaxies

Emission Line Galaxies (ELGs), contrary to LRGs, have a high rate of star formation. These newly formed stars interact with the interstellar gas surrounding them, producing the prominent emission lines that characterize these galaxies. DESI expects to observe around 17.1 million ELGs.

The redshift range for ELGs will be $0.6 < z < 1.6$. The estimation strategy for ELGs is based on a characteristic Ionized Oxygen [OII] double emission lines at 3700 Å on their spectra at rest frame (see fig. 2.6), see section 3.3 of DESI Collaboration et al. (2016a) for more details.

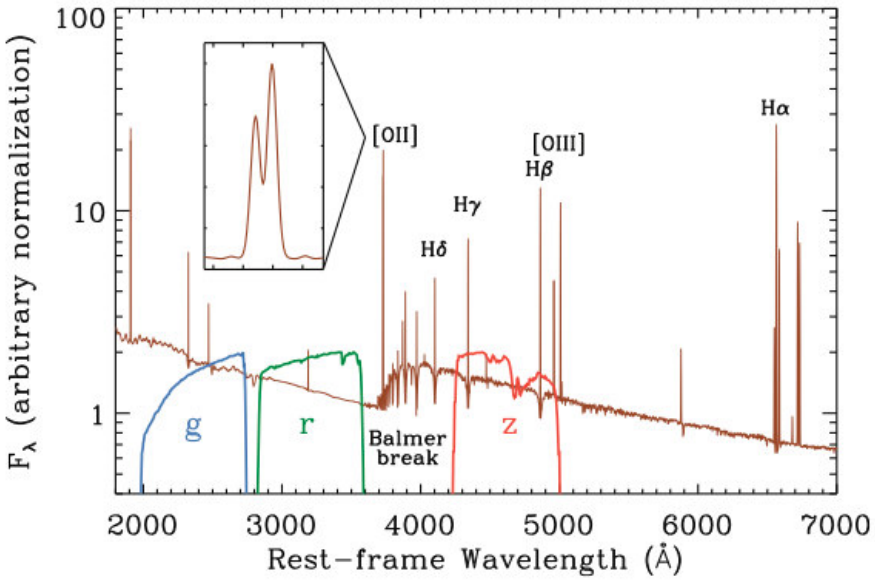


**Figure 2.6:** Example rest frame spectra of an Emission Line Galaxy (ELG), the inset shows the characteristic double emission lines from Ionized Oxygen [OII] at 3700 Å. Figure taken from DESI Collaboration et al. (2016a).

### Quasars

QSOs are the highest redshift target in the DESI survey, they will be used to trace matter clustering. Around 1.7 million QSOs with a redshift range from $0.9 < z < 2.1$ will be used as direct tracers. Also, up to 0.7 million Lyman-Alpha (Ly-$\alpha$) QSOs with redshift $z > 2.1$, will be used to trace matter indirectly through the Ly-$\alpha$ Forest.

The strategy to identify QSOs and estimate their redshift is through emissions from three-times and two-times ionized Carbon [CIV] and [CIII], respectively; ionized Magnesium [MgII], Ly-$\alpha$, two-times ionized Oxygen [OIII] and H-$\alpha$ in their spectrum (see fig. 2.7).

All the QSOs will be observed once on the early stages of the survey, those confirmed to have a redshift $z > 2.1$ will be re-observed up to four times.

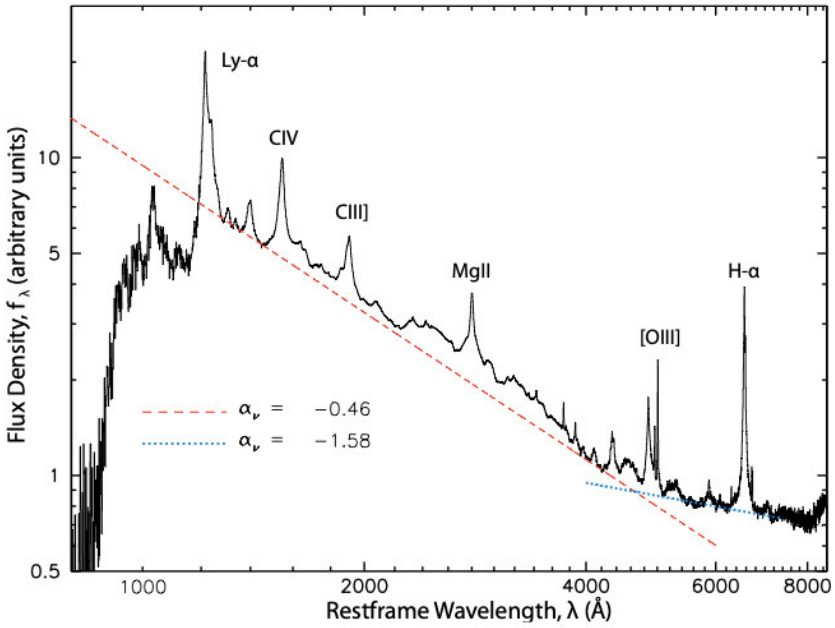


**Figure 2.7:** Example quasar (QSO) spectrum. This spectrum shows some characteristic emission lines from quasars, such as three-times and two-times ionized Carbon [CIV] and [CIII], ionized Magnesium [MgII], Lyman-$\alpha$, two-times ionized Oxygen [OIII] and H-$\alpha$. This emission lines will be used to identify QSOs and estimate their redshift. Figure taken from DESI Collaboration et al. (2016a).

## 2.3 The Legacy Imaging Surveys

The selection of the targets mentioned above requires a previous imaging survey. This imaging survey was done by *The DESI Legacy Imaging Surveys*, hereafter referenced as the Legacy Surveys, a set of three projects, the Dark Energy Camera Legacy Survey (DECaLS), the Beijing-Arizona Sky Survey (BASS) and the Mayall z-band Legacy Survey (MzLS), that started operations in August 2014 and finished in March 2019.

The Legacy Surveys observed altogether the 14,000 $\deg^2$ of what its defined as *DESI's footprint*, covering those areas within $|b| > 18°$ in Galactic coordinates and $-18° <$ DEC $< 84°$ in celestial coordinates, with three optical bands ($g$, $r$ and $z$) optical bands and an inclusion of the imaging data from the Wide-field Infrared Survey Explorer (WISE) satellite (Wright et al., 2010). The footprint covered by the Legacy Surveys is shown in fig. 2.8, this figure also contains information about the status of the observations in the $g$-band.

This section is dedicated to give a brief description of the three surveys and the WISE satellite.

### Dark Energy Camera Legacy Survey

The Dark Energy Camera Legacy Survey (DECaLS) operated from August 2014 to March 2019 with the Dark Energy Camera (DECam) located on the Blanco 4-m telescope in the Cerro Tololo Inter-American Observatory in the Coquimbo Region, Chile.

This survey covered $\sim$ 9000 $\deg^2$ DESI footprint, in the Northern Galactic Cap (NGC) at DEC$\leq 32°$ and the Southern Galactic Cap (SGC) at DEC$\leq 34°$ with the $g$, $r$ and $z$ optical bands. DECaLS also includes data sets from the Dark Energy Survey (DES; The Dark Energy Survey Collaboration, 2005) of $\sim$ 5000 $\deg^2$ in the SGC, this area was not re-imaged by DECam.

### Beijing-Arizona Sky Survey

The Beijing-Arizona Sky Survey (BASS), began observations in January 2015 and concluded in March 2019 using the 90Prime camera at the prime focus of the Bok

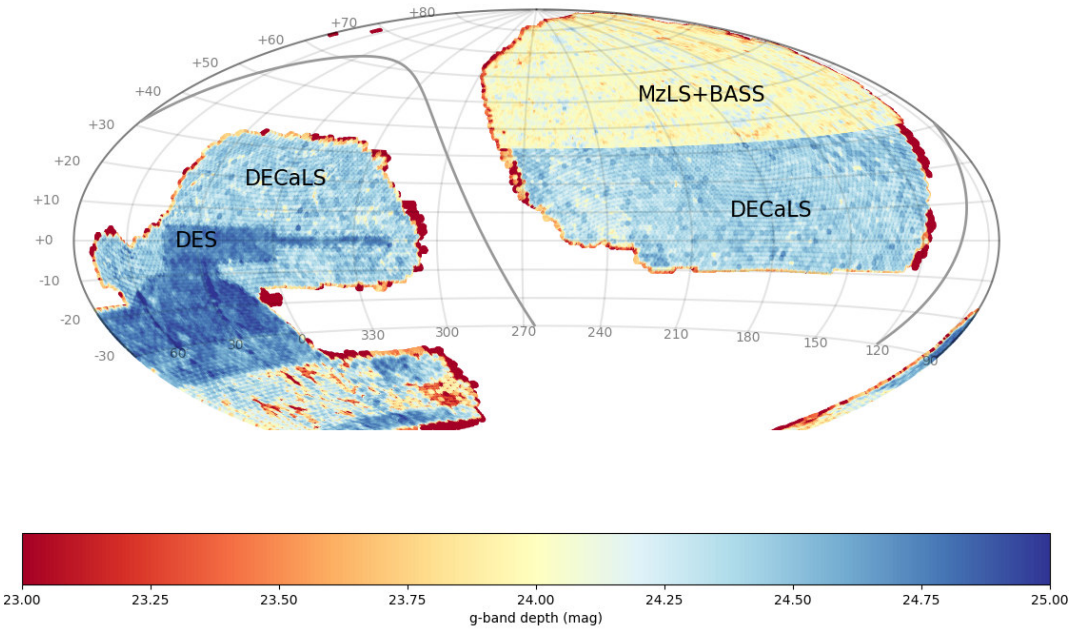


**Figure 2.8:** Footprint of the DESI Legacy Imaging Surveys. This figure also shows the status of the DESI Legacy Imaging Surveys in the $g$-band as of Data Release 8 (DR8), July 2019. The colors show the magnitude depth, corrected by galactic extinction. The solid line shows the galactic plane. Figure taken from the DESI Legacy Imaging Surveys status public website, http://legacysurvey.org/status. The figures for the $r$ and $z$ bands can be found in this same website.

2.3-m telescope in Kitt Peak, Arizona. BASS covered an area of $\sim 5000\,\mathrm{deg}^2$ on the regions with DEC$\geq 32°$ in the DESI footprint with the $g$ and $r$ optical bands.

### Mayall z-band Legacy Survey

The Mayall z-band Legacy Survey (MzLS) began observations in February 2016 and officially ended in February 2018. MzLS covered $\sim 5000\,\mathrm{deg}^2$ of the DESI footprint regions with DEC$\geq 32°$ using the $z$-band optical band, complementing the BASS observations. This survey was done using the MOSAIC-3 camera at the 4-m Mayall telescope in Kitt Peak, Arizona.

### Wide-field Infrared Survey Explorer

The Wide-field Infrared Survey Explorer (WISE; Wright et al., 2010) is an Infrared space telescope, designed and supervised by NASA launched in December 2019 and began observations in January 2010. The WISE observations were done by four Infrared bands centered a 3.4, 4.6, 12 and 22 µm, known as W1, W2, W3 and W4. The Legacy Surveys include the data from the two lowest bands from WISE (W1 and W2).

## 2.4 Scientific Goals

DESI will study the effects of the Dark Energy on the expansion of the Universe through BAO, also it will measure the growth of structure using the Redshift Space distortions. In this section some numbers of the precision required for DESI to achieve its goals wil be given. This section is mainly based on section 2 of DESI Collaboration et al. (2016a) and the Science Requirement Document (DESI Collaboration).

To achieve its scientific goals DESI will measure the spectra of approximately 30 million targets in its $14{,}000\,\mathrm{deg}^2$ footprint during a five-year period, just as a comparison, previous experiments dedicated to study the Universe expansion history through BAO like the Baryon Oscillation Spectroscopic Survey (BOSS; Dawson, Schlegel, et al., 2013) altogether with its extended version (eBOSS; Dawson, Kneib, et al., 2016), observed an area of $10{,}000\,\mathrm{deg}^2$ and collecting the spectra of nearly 3 million objects, an order of magnitude below DESI!

If the whole 14,000 deg$^2$ area is covered, DESI expects to measure the BAO scale with 0.22% and 0.31% precision for redshifts $z < 1.1$ and $1.1 < z < 1.9$, respectively. Additionally, DESI will measure the Hubble parameter $H(z)$ with 0.84% for redshifts $1.9 < z < 3.7$ by fitting the position of the BAO scale in the Lyman-$\alpha$ forest auto-correlation and the Lyman-$\alpha$ forest-quasar cross-correlation. Also, the growth of structure will be measured by the factor $f\sigma_8$, for redshifts $0.5 < z < 1.6$ with a precision of few percent.

The projected DESI measurements with its errors for the Hubble parameter and the BAO scale as a function of redshift are shown in the left and right panel of fig. 2.9, respectively.

Although the main goals of DESI are mainly based on BAO and the Redshift Space Distortions, the data obtained will provide the tools to constrain inflation and the sum of the neutrino masses with a few percent error, improving the measurements done by other experiments such as Planck (Planck Collaboration et al., 2018).

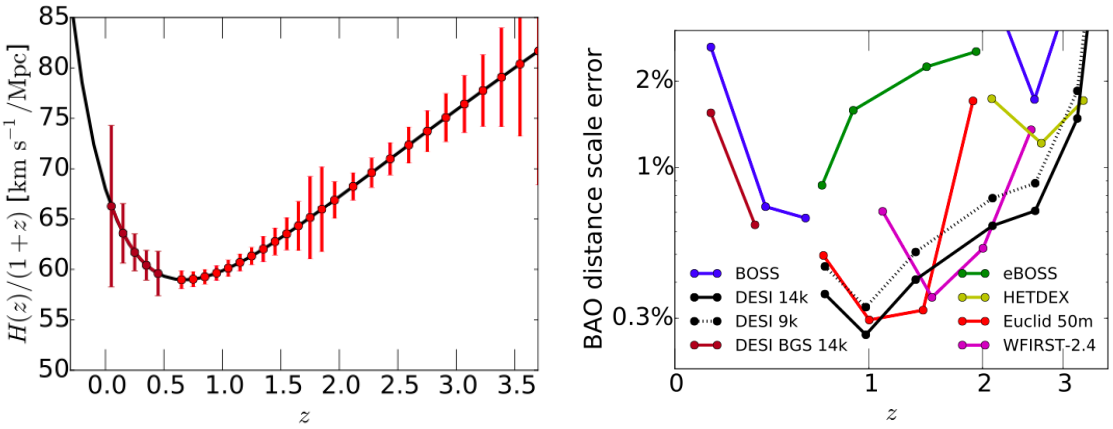


**Figure 2.9:** Left: Forecast of errors of DESI on the Hubble parameter as function of the redshift. Right: Comparison of the fractional error on the BAO scale of DESI with other experiments. Figures taken from DESI Collaboration et al. (2016a).

To close this chapter, it must be remarked that the feasibility of the target type sample sizes and the measurement precision discussed in section 2.2 and the previous section, respectively, can be tested through the analysis of simulated data of DESI's observations. This motivates the next chapter, where a pipeline dedicated to the simulation of the first year of DESI's Lyman-$\alpha$ quasars observations will be discussed.

# 3

# Mock data of DESI's first year

The main purpose of this thesis is to generate a simulation of the quasar spectra that DESI will observe during its first year of operations.

Ideally, the DESI Lyman-$\alpha$ forest working group would like to have a database that contains mostly the spectra of those Lyman-$\alpha$ quasars observed during the first year of DESI's operations. A way to achieve this, is to do a simulation of the whole survey during the first year. However, this is a computationally expensive process.

An alternative is to do a survey planning simulation, simulate the targets selected to be observed, get the amount of observed quasars and how many times they were observed. Then, the footprint, quasar density and number of observations can be mimicked with a dedicated script that generates Lyman-$\alpha$ quasar spectra.

This task requires the adaptation and connection of different codes of the DESI collaboration (`desicode`), publicly available in https://github.com/desihub, to follow the pipeline described in fig. 3.1.

This chapter will describe these codes, their functionality and contributions to achieve the simulation of DESI's first year, along with the results obtained.

## Previous definitions

Prior to describe the process of simulating DESI's first year of observations, some terms that will be used along this chapter must be defined.

- **Tile:** DESI's footprint can be split into *tiles*, these correspond to a circle of 1.606 deg radius that the projection of the focal plane system prints in a given position of the sky. The whole footprint of DESI can be covered by 2,000 tiles,

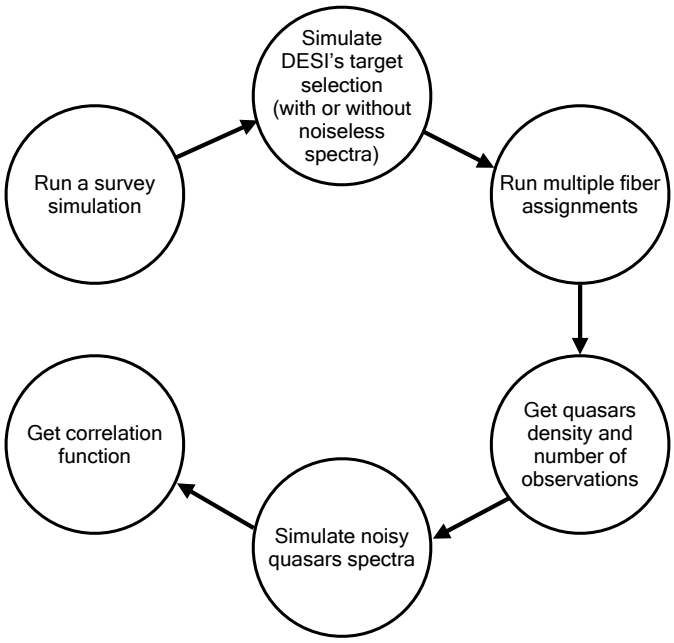


**Figure 3.1:** Pipeline followed to build the simulation of DESI's first year quasar observations.

with a little overlap.

- **Layer:** A *layer* is referred to a whole coverage of DESI's footprint by 2,000 tiles. DESI's footprint will be covered by four and three layers of the dark time and bright time programs, respectively. There will be also a layer called "gray", that will be covered during the time of the night that has less luminous contamination than the bright program but is not optimal for the dark program, giving a total of 8 layers and 16,000 tiles.

- **HEALPix pixel:** HEALPix is the acronym for **H**ierarchical **E**qual **A**rea iso**L**atitude **Pix**elization (Górski et al., 2005). As its name states a HEALPix, is a division of the surface of a sphere into equal sized sub-areas, called pixels.

  The base resolution of a HEALPix pixel, from now on referenced just as pixel unless otherwise indicated, is such that the sphere is split into 12 equal sized pixels. The rest of the resolutions are expressed into another useful definition, $N_{\rm side}$, that states the number of divisions in the side of a base resolution pixel, therefore, the sphere is split into $12N_{\rm side}^2$ pixels, the *nside* is such that $N_{\rm side} = 2^k$, where $k$ is the resolution parameter, the area of each pixel $\Omega_{\rm pix}$ is such that

$\Omega_{\text{pix}} = \pi/(3N_{\text{side}}^2)$ in sterad or $\Omega_{\text{pix}} = 10,800/(\pi N_{\text{side}}^2)$ square degrees.

- **FITS file:** The **F**lexible **I**mage **T**ransport **S**ystem (Wells et al., 1981), is a file format designed to store astronomical data. A FITS file usually contains multiple readable headers with useful information for the user, also it can contain images or tables with multiple rows and columns with a given name.

## 3.1 Survey simulation

First, a simulation of the survey planning must be done, this can be achieved by the `desisurvey` and `surveysim` modules, available in https://github.com/surveysim and https://github.com/desisurvey, respectively. For the purpose of this thesis, previous realizations of the survey simulation done by other members of the DESI collaboration were used.

Basically, a survey simulation generates random weather conditions during a period of observations, then the scheduling of each tile during this period is set based on these conditions.

The survey simulation is done by two scripts within the submodules: `surveyinit` and `surveysim`. They require a configuration file that sets the parameters for the planning and scheduling of the survey. An example of a configuration file can be found in https://github.com/desihub/desisurvey/blob/master/py/desisurvey/data/config.yaml, this document is self explained and most likely the parameters inside it, besides the first and last day of the survey, should not be changed unless some experiments are being tested.

The output from a survey simulation include several FITS files with the ephemerides from 2019 to 2025, the estimated weather, and a table with the tile exposures in time order. More information about the outputs of the survey simulations can be found in https://desidatamodel.readthedocs.io/en/latest/DESISURVEY_OUTPUT/index.html

## 3.2 Target selection

A database of the available targets in the sky that fulfill DESI's observation requirements is required. This can be simulated using the `select-mock-targets` (SMT),

script from the `desitarget` module, available in https://github.com/desihub/desitarget/blob/master/bin/select_mock_targets.

Originally, SMT simulates the target selection and spectra by adding noise to predefined templates. The latter can be skipped with an option within the script reducing considerably the computing time, however the inclution (or not) of this option causes a change on the magnitude distribution of the targets selected, a possible explanation is that the noise added to the spectra template somehow alters the target selection criteria causing this change, but it is still on discussion.

The functionality of SMT requires a configuration file which sets the target types and density that will be simulated, an example can be found in https://github.com/desihub/desitarget/blob/master/py/desitarget/mock/data/select-mock-targets.yaml. For the main purpose of this thesis, the simulation consisted of QSO targets with $z < 1.8$ with a density of $120\,\mathrm{QSO}/\,\mathrm{deg}^2$, Lyman-$\alpha$ QSO targets with $z > 1.8$ with a density of $50\,\mathrm{QSO}/\,\mathrm{deg}^2$, stars within the Milky Way Galaxy and sky targets for calibration.

SMT stores the following FITS files organized by pixel:

- A targets file, that contains information from each objective, such as the target's Right Ascension and Declination, flux, priority of observation (to be used in fiber assignment), target number of identification (TARGETID), just to mention some. For more information refer to https://desidatamodel.readthedocs.io/en/latest/DESI_TARGET/targets.html.

- A truth file, that contain the targets true data, such as redshift, target type and flux, also it includes the TARGETID to match with the targets file.

- A sky file, that contains the same information as the targets file, for blank sky locations, this is used for calibration.

The first two are divided into two files, one for each observation program (bright and dark). These files were merged into a single file of targets, truth and sky files, the former is referenced within the collaboration as Merged Target List (MTL).

## 3.3 Fiber assignment

As mentioned in chapter 2, DESI's focal plane system contains 5,000 fibers to observe different targets at the same time. Each fiber is assigned to a target by the scripts within the `fiberassign` module (https://github.com/desihub/fiberassign) based on a priority system, where Lyman-$\alpha$ QSOs have the highest priority while ELGs have the lowest priority during dark program observations.

The `fiberassign` script requires as an input an MTL and a sky files, also as an optional argument the set of tiles from which the fibers will be assigned can be given. The output is a group of FITS files, one for each observed tile, that contain information about the targets to which each fiber was assigned, more information can be found in https://desidatamodel.readthedocs.io/en/latest/DESI_TARGET/fiberassign/tile-TILEID-FIELDNUM.html.

In this step the output from the survey simulation is connected with the targets generated by SMT. The idea is to do a monthly iteration of the fiber assignment script following the tile observing schedule from the survey simulation in the selected targets. This iteration is done by the `multipass`, available in the GitHub repository https://github.com/HiramHerrera/multipass/blob/mymultipass/run_multilayer.py, this is an adaptation of the original script, written by Jaime Forero, which can be found in https://github.com/forero/multipass.

Essentially this version of `multipass`, requires the same files as `fiberassign` and an optional exposures file, which will dictate the sequence of the tiles to observe each month, this file is the same as the outputs from the survey simulations. The script is constructed such that the MTL file and a redshift file are updated and saved into memory every iteration. The final output is a file that contains the redshift, positions, target type and number of observations of each observed object during the period dictated by the exposures file.

## 3.4 Density file

With the outputs from `multipass` a FITS file that contains the quasar density and the number of observations probability for each pixel can be constructed, to do so the following steps are required:

i. Select only the QSO targets in the data set.

ii. Separate the QSOs into three different redshift regions:

- **Low z:** $z < 1.8$.
- **Mid z:** $1.8 < z < 2.1$.
- **High z:** $z > 2.1$.

iii. Group the QSOs by pixels based on their positions.

iv. Get the QSO density for each redshift region and each pixel, this is done by dividing

$$\rho_{\text{pix}}(z) = \frac{N^{\text{pix}}_{\text{QSO}}(z)}{\Omega_{\text{pix}}} \tag{3.1}$$

where $N^{\text{pix}}_{\text{QSO}}(z)$ is the number of quasars in the pixel within a given redshift region. For this work a value $N_{\text{side}} = 16$ was used, this corresponds to a pixel area of $\Omega_{\text{pix}} \sim 13.43\,\text{deg}^2$.

The results for the simulation of DESI's first year footprint and the quasar density for each redshift region are shown in fig. 3.2, the total number of quasars for each redshift region is shown in table 3.1. The number of quasars and densities obtained are consistent with DESI's science requirements.

**Table 3.1:** Total number of quasars obtained for DESI's first year simulation.

| **Redshift region** | $\boldsymbol{N_{\text{QSO}}}$ |
|---|---|
| $z < 1.8$ | 648,710 |
| $1.8 < z < 2.1$ | 211,778 |
| $z > 2.1$ | 387,666 |
| **Total** | 1,248,154 |

v. Get the probability for a quasar with $z > 2.1$ to have $N$ observations in a given pixel, this probability is obtained

$$P_{\text{obs}} = \frac{N^{\text{pix}}_{\text{QSO,Nobs}}(z > 2.1)}{N^{\text{pix}}_{\text{QSO}}(z > 2.1)}, \tag{3.2}$$

where $N^{\text{pix}}_{\text{QSO,Nobs}}(z > 2.1)$ denotes the number of quasars with $z > 2.1$ with $N$

observations.

The results for the simulation are shown in fig. 3.3 where it can be seen a progression where most of the quasars are observed one time.

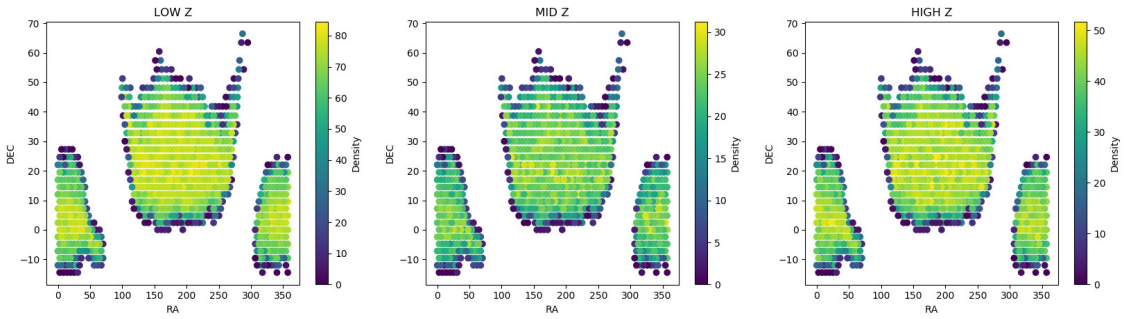


**Figure 3.2:** Footprint of DESI's first year as obtained by `multipass`. Colors indicate the quasar density of each pixel. Panels are divided into three redshift regions: **Low z:** $z < 1.8$, **Mid z:** $1.8 < z < 2.1$ and **High z:** $z > 2.1$.

## 3.5 Quasar spectra

The script dedicated to simulate Lyman-$\alpha$ quasars spectra is `quickquasars`, from the `desicode` submodule `desisim`, available in https://github.com/desihub/desisim. This script can generate thousands of spectra in a few minutes with different degrees of realism, it can include absorbers such as BALs, DLAs and metals, discussed at the end of section 1.3.1.

The current version of `quickquasars`, simulates a set of pixels with the same density of quasars and all of them have the same exposure time, this doesn't reflect the reality of DESI's observations, hence this script must be modified.

This is the main contribution of this work to the DESI collaboration: the modification of `quickquasars` so that it can generate a certain number of pixels with different quasar densities and these quasars have multiple exposure times. These modifications can be found in a branch of a forked repository of `desisim`, called `multiexposures`, available in https://github.com/HiramHerrera/desisim/tree/multiexposures, these consist mainly in two additions to the sub-module:

- The creation of a new script that reads the information from the density file created during the previous section. This script essentially uses the densities

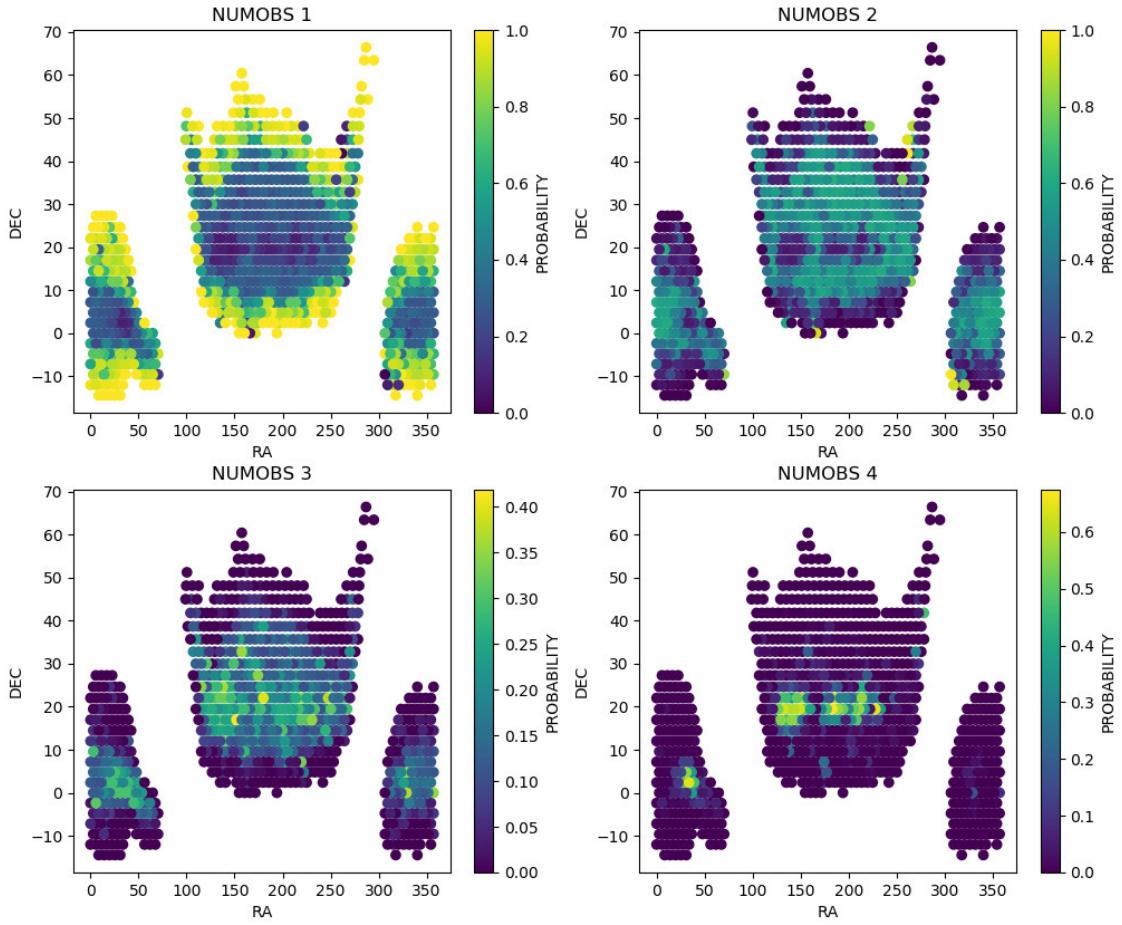


**Figure 3.3:** Number of observations probability as obtained by `multipass`. Each panel represents the probability of having a certain number of observations on a given pixel, from one up to four.

to select a number of quasars to be simulated for each redshift region, then assigns a random number of observations to each quasar with redshift $z > 2.1$ based on the probabilities of having $N$ observations in that pixel, for those quasars with redshift $z < 2.1$ it assigns one observation (exposure time of 1000 seconds).

Also, if the desired pixel to simulate does not belong to any of those present in the density file, this script skips the process. It is important to assert that the footprint in this density file is not necessarily that of DESI's first year, it can be whatever footprint the user likes to simulate. The main routine to create the density file can be found in this script too.

By the moment I'm writing this thesis this script is called `fpsubsample`, as for ***f**oot**p**rint subsample*.

- The addition of some code lines to the main `quickquasars` script so it is compatible with `fpsubsample`. A feature in this version is that the footprint in the density file can be simulated with either all the quasars having the same number of observations or with multiple exposure times according to the probabilities, this is done mainly for comparing the output spectra from two realizations of the same footprint.

This version of `quickquasars` was used to generate the spectra of quasars without BALs, DLAs and metals and redshift $z > 1.8$ in DESI's first year footprint based on the results of fig. 3.2 and the probabilities from fig. 3.3. A density file was constructed from the results of these realizations to be compared with the output from `multipass`, the results for the quasar density and number of observations can be seen in fig. 3.4 and fig. 3.5.

The density of quasars obtained for the **Mid z** and **High z** regions is the same in both version of the simulation, the number of observations probability vary a little, but they follow the same distribution. This can be seen more clearly in fig. 3.6, where the probability distribution of the pixels for both runs (`multipass` and `quickquasars`) are shown.

Four examples of the quasar spectra generated by `quickquasars` are shown in fig. 3.7, this figure compares the spectra obtained by a simulation of the first year of DESI's observations with multiple exposure times with a simulation of the same footprint

but where all the quasars have one observation, this translates into an exposure time of 1000 seconds, this realization will be referred as BASE. In the figure it is seen that the spectra generated by both runs has its emission lines placed equally and the differences between them are due by the exposure time only.

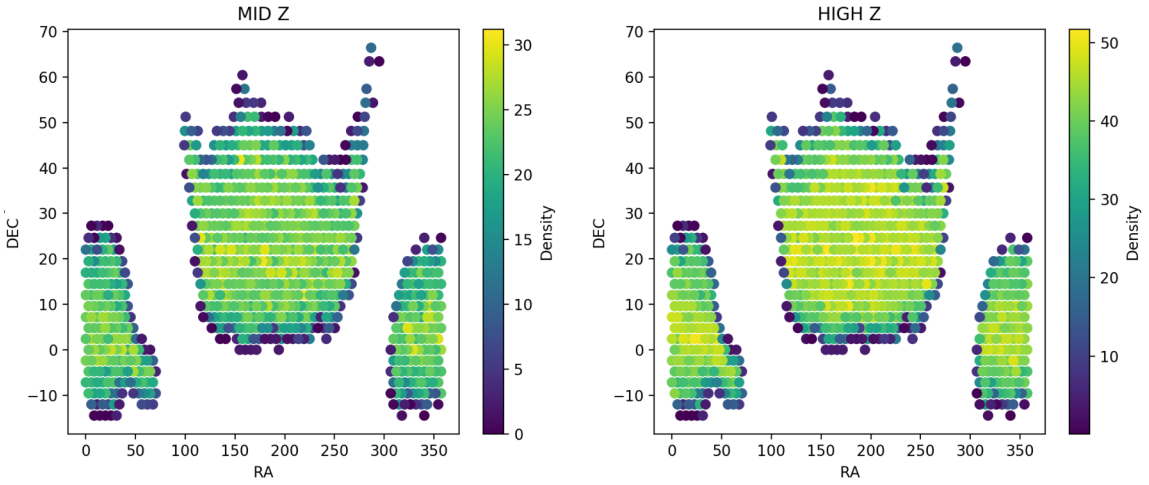


**Figure 3.4:** Same as fig. 3.2, but for the output QSO density from `quickquasars`. In the figure QSOs in the **Low z** region are not shown since `quickquasars` was run so it only generated quasars with redshift $z > 1.8$.

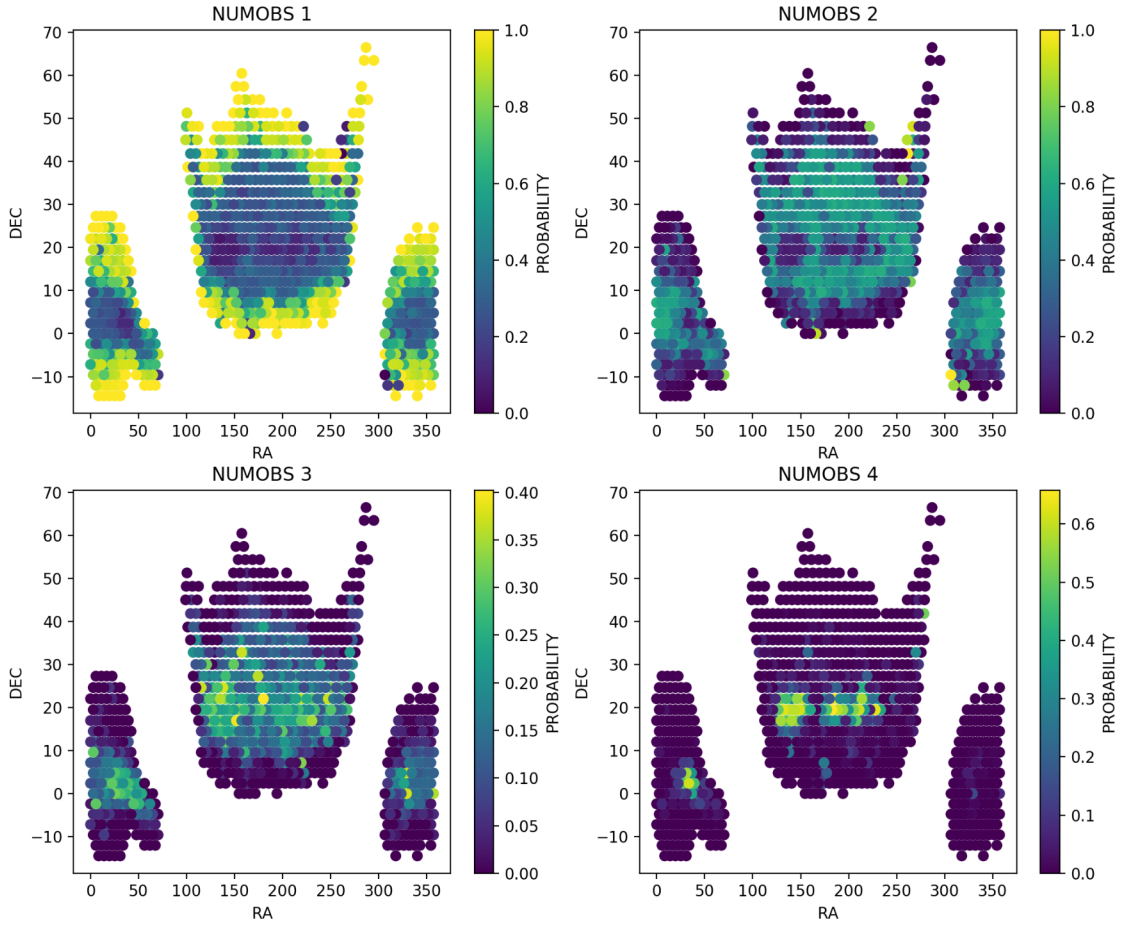


**Figure 3.5:** Same as fig. 3.3 but for the `quickquasars` output.

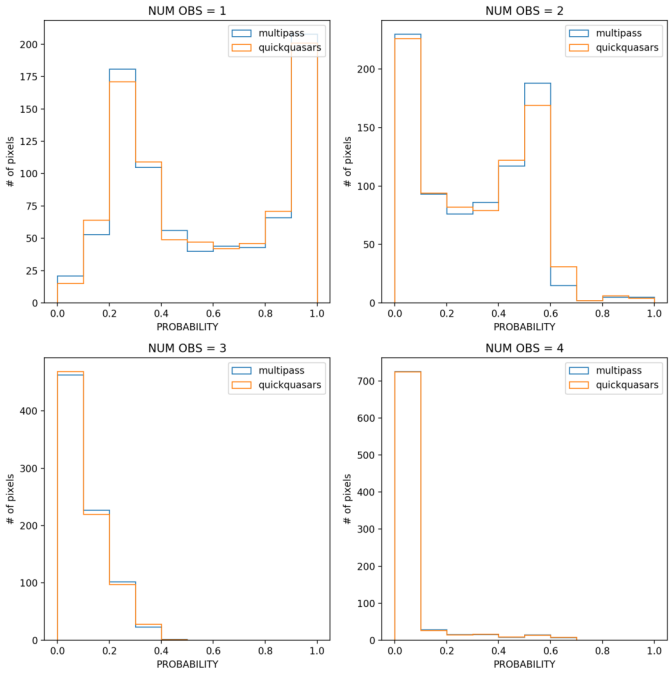


**Figure 3.6:** Histogram of the number of pixels with a given probability of having $N$ observations, from one up to four, the probabilities divided on bins of size 0.1. In all panels the results for `multipass` (blue) and `quickquasars` (orange) are shown.

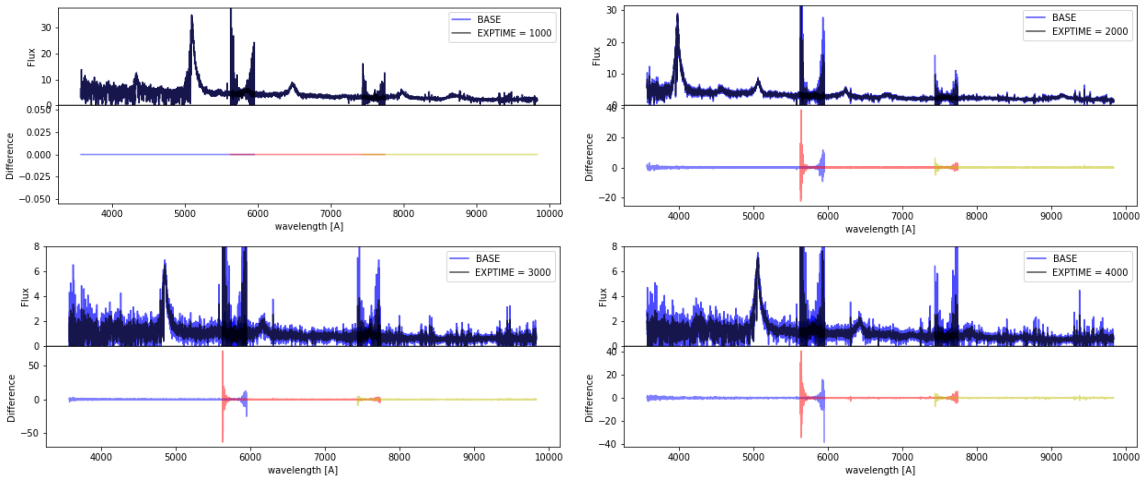


**Figure 3.7:** Quasar spectra simulated by `quickquasars`. Each panel shows on top a quasar spectrum with a give number of observations (from one up to four) compared with the original spectrum (BASE) with only one observation and on the bottom the difference between the two spectra, the colors on the bottom represent DESI's spectrograph wavelength channels. Each observation represents 1000 seconds of exposure time.

## 3.6 Correlation function

With the quasar spectra generated the three-dimensional correlation function can be measured as described in section 1.3.2. To do so, the **P**ackage for **I**GM **C**osmological-**C**orrelations **A**nalyses (`picca`), available in https://github.com/igmhub/picca, was used.

A flat ΛCDM model with $\Omega_m = 0.3147$ (Planck Collaboration et al., 2018) was assumed in order for `picca` to compute the correlation function by converting the angles (RA and DEC) and redshift, $z$, of a given slice of redshift $z$ within the quasar spectrum into co-moving positions.

The results of the Lyman-$\alpha$ forest auto-correlation and the Lyman-$\alpha$ forest and quasars cross-correlation at an effective redshift $\bar{z} = 2.34$, divided into four ranges of $\mu = r_{\parallel}/r$ for both runs of `quickquasars` (multiple exposures and BASE), are shown in fig. 3.8 and fig. 3.9, respectively. For the scope of this thesis, a fitting of the BAO peak position is not necessary.

There are some differences on the auto-correlation and cross-correlation functions relative to the BASE realization, however, the interest of this work is the improvement of the error bars in the correlation function by the multiple exposures simulation, this is done by calculating the fractional difference between the two realizations:

$$\Delta\text{Error} = 1 - \frac{\text{Error}(\text{r}^2\xi_{\text{ME}}(\text{r}))}{\text{Error}(\text{r}^2\xi_{\text{BASE}}(\text{r}))}, \tag{3.3}$$

where $\text{Error}(\text{r}^2\xi_{\text{ME}}(\text{r}))$ and $\text{Error}(\text{r}^2\xi_{\text{BASE}}(\text{r}))$ represent the magnitude of the error bars at a given radius $r$ for the Multiple Exposures and BASE runs, respectively.

The improvement in the Lyman-$\alpha$ forest auto-correlation error bars is shown in fig. 3.10, while the improvement for the Lyman-$\alpha$ forest and quasars cross-correlation is shown in fig. 3.11. The mean improvement for all the four $\mu$ ranges for both auto-correlation and cross-correlation is shown in table 3.2.

To close this chapter the following must be discussed:

- For the test done in this thesis where the targets used were quasars, Lyman-$\alpha$ quasars and stars, there were no issues (in computational terms). However, if more tests including more types such as ELGs and LRGs were required a

**Table 3.2:** Mean Improvement on the auto-correlation and cross-correlation for all the four $\mu = r_{\parallel}/r$ ranges.

| | $0 < \mu < 0.5$ | $0.5 < \mu < 0.8$ | $0.8 < \mu < 0.95$ | $0.95 < \mu < 1$ |
|---|---|---|---|---|
| **auto-correlation** | 0.2112 | 0.2022 | 0.1944 | 0.1909 |
| **cross-correlation** | 0.1082 | 0.1040 | 0.1040 | 0.1051 |

memory issue would arise when trying to construct the merged truth, sky and MTL files. A possible solution is to extract from the MTL only those columns required by the fiber assign code and work with this reduced MTL.

- The vast majority of the time consumed while implementing this pipeline is on the fiber assignment, more specifically on the iterations done by multipass, consuming up to 50 minutes of real computer time by each iteration. Also there might be some memory errors while this process is active, this is being worked on. The current way to work around this issue, is that the code is structured such that if a realization is interrupted the files produced during the iterations are used to resume it.

- The results obtained in section 3.4 show a footprint obtained from a survey simulation scheduled with given random weather conditions. The real DESI's first year footprint will depend on the actual weather conditions of the year.

- The fiber assignment and target re-observation strategies are still on discussion and are subject to changes, these changes would possibly imply a different number of observation probabilities.

- Related to the previous point, the pipeline developed is self-consistent, meaning that these possible changes in the strategies can be reflected on the simulation of DESI's year one Lyman-$\alpha$ quasar observations easily through the survey simulation and fiber assignment codes once these changes are implemented.

- The improvement on the error bars of the correlation function is expected to be of the same order,independently of the weather conditions used, even if there are BALs, DLAs or metals included. However, as stated in the second point of this list, if the strategies change, this would possibly produce a change in the number of observations probabilities, and therefore on the improvement of the correlation function error bars.

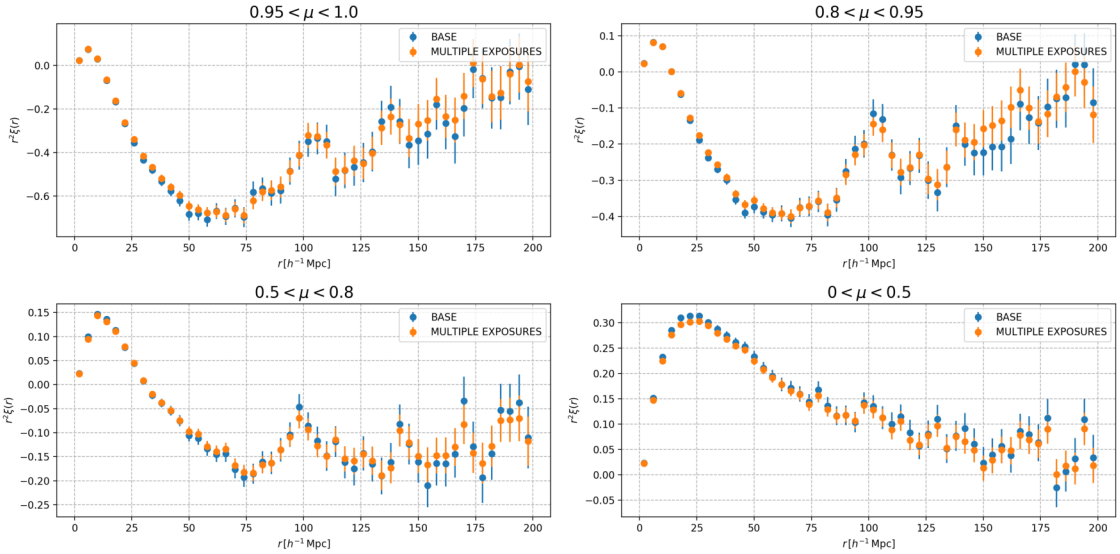


**Figure 3.8:** Lyman-$\alpha$ forest auto-correlation in four ranges of $\mu = r_{\parallel}/r$ for two runs of `quickquasars`, one having multiple exposures (orange) and a BASE run where all the quasars have a exposure time of 1000 seconds (blue).

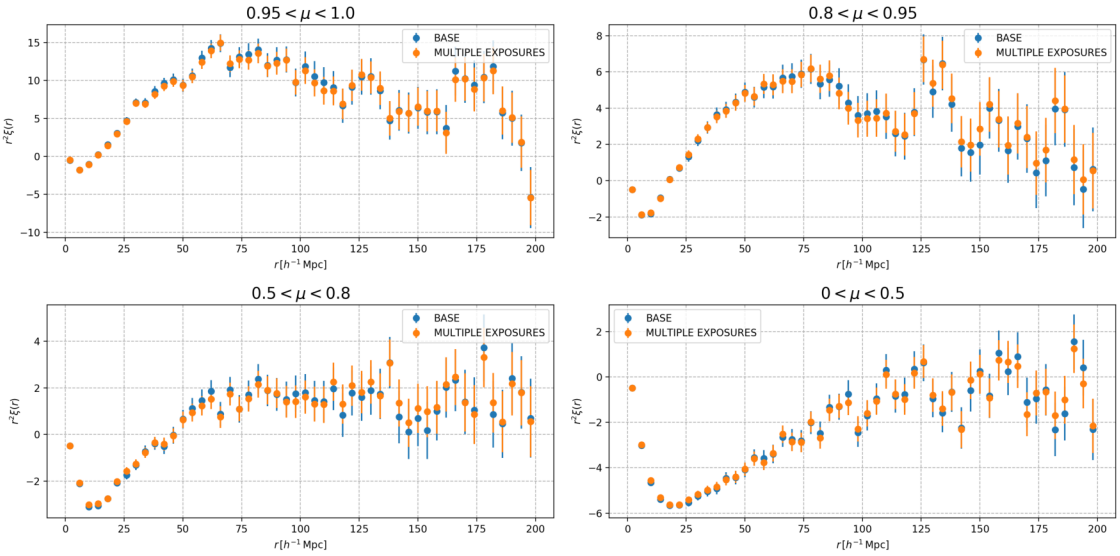


**Figure 3.9:** Same as fig. 3.8, but for the Lyman-$\alpha$ forest and Quasars cross-correlation.

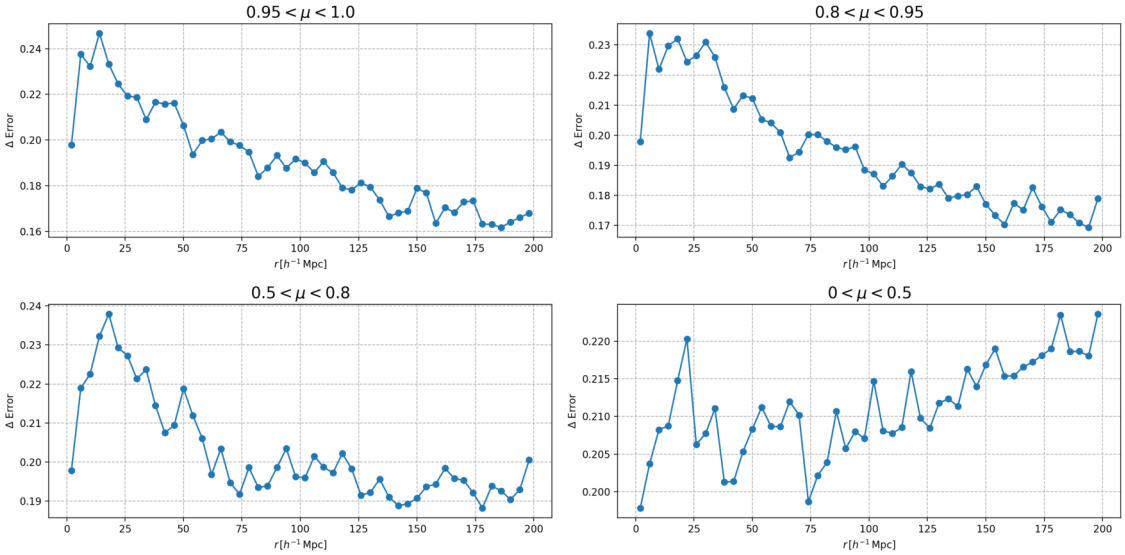


**Figure 3.10:** Improvement on the error bars (in four $\mu = r_{\parallel}/r$ ranges) by the run of `quickquasars` where quasars have multiple exposures compared to the BASE run where all the quasars have 1000 seconds of exposure time, the improvement is calculated by eq. (3.3).

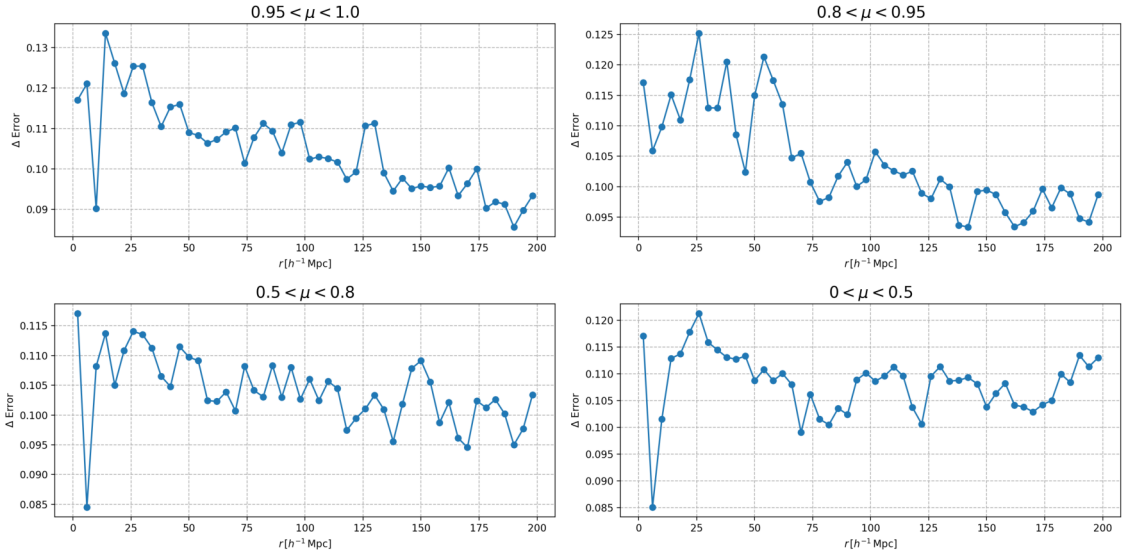


**Figure 3.11:** Same as fig. 3.10, but for error bars of the Lyman-$\alpha$ forest and Quasars cross-correlation.

# 4 Conclusions and Future work

As mentioned in chapter 1 BAO provides a standard ruler that can be used to study the Universe's expansion history and constrain cosmological models, a way this can be achieved is through Lyman-$\alpha$ forest and the measurement of the correlation function. The precision of the measurement of the correlation function is highly related with the sample size of a spectroscopic survey, this motivates the development of larger galaxy spectroscopic surveys.

The size of the spectroscopic surveys has evolved exponentially over the pass of the years. The first of the next generation surveys, is the Dark Energy Spectroscopic Instrument (DESI) which will provide a 30 million galaxy sample.

In chapter 2 the scientific goals of DESI were discussed, these include a measurement of the Hubble parameter with 0.84% precision by fitting the BAO peak position in the correlation function constructed from 1.7 million quasars and 0.7 million Lyman-$\alpha$ quasars that will be measured by DESI.

The expected quasar density and precision of the measurement of the Hubble parameter can be tested by the usage of simulations. The scope of this work is to simulate the Lyman-$\alpha$ quasars observations of DESI during its first year of observations. To achieve this task a straight forward pipeline was developed. This pipeline includes the simulation of the scheduling of the survey by generating random weather conditions, the selection of mock targets that fulfill DESI's science requirements, the assignment of the instrument fibers to observe this targets, the simulation of the Lyman-$\alpha$ quasars spectra based on a footprint and number of observations and the measurement of the correlation function.

The simulation of DESI's first year of Lyman-$\alpha$ quasar observations required the adaptation and connection of multiple codes from the `desicode`. Including a modi-

fication of the dedicated Lyman-$\alpha$ quasars spectra simulation code, `quickquasars`, this is the main contribution of this work to the DESI collaboration, a fully functional version of this script that can simulate a given footprint with different quasar densities and multiple exposure times.

As it was discussed in chapter 3, a simulation of a footprint of DESI's first year was achieved, however the actual footprint that DESI will measure is subject to the weather conditions during the year. Therefore more realizations with different weather conditions must be done in order to reduce systematic errors on the measurements.

With the footprint obtained there were produced two simulations of the Lyman-$\alpha$ quasars spectra without including contaminants such as DLAs, BALs and metals, discussed in section 1.3.1. One of these simulations was done with multiple exposure times and in the other all the quasars have one observation, the latter was referred as BASE during this work. More realizations including contaminants must be done in order characterize the possible systematic errors.

By comparing the error bars of the multiple exposures simulation with the ones of the BASE simulation there was found an improvement of $\sim$20% and $\sim$10% in the Lyman-$\alpha$ forest auto-correlation and Lyman-$\alpha$ forest-quasar cross-correlation functions, respectively. This makes sense since the error correlation function is directly related with the variance of the Lyman-$\alpha$ forest flux fluctuations, having more exposure time on the quasars spectra and therefore, lower noise reduces the value of $\delta_q$ in eqs. (1.31) and (1.32) leading to a reduction of the error bars. It is expected that the improvement in the error bars of simulations including BALs, DLAs and/or metals, has the same magnitude as the ones presented in this work.

It is important to remark that the results obtained are subject to changes. Since the DESI collaboration is discussing the fiber assignment and target re-observation strategies, this affects directly the results obtained by possibly changing the year one footprint and number of observations distribution. As stated at the end of chapter 3, the pipeline developed during this work is self-consistent and these changes should be reflected as soon as the fiber assignment and survey simulation codes implement these changes.

As a future work, apart from the runs including different degrees of realism with DLAs, BALs and metals and a combination of them, multiple realizations of these

simulations with different conditions will be generated. These will help to forecast the possible results of DESI and will help us to study the systematic errors on the data analysis. DESI just started operations so there is still a lot of work to be done during the five-year period it will operate!

# Acknowledgments

First, I would like to thank my advisor Alma for introducing me to DESI and the Lyman-$\alpha$ forest working group, also for motivating me during this work, this would have not been possible without her guidance.

To my posgraduate friends who are also involved in DESI Oleg and Andrea for their answers and discussion to my questions about programming and astronomy, respectively.

Also, to those friends who even that the are not involved with DESI they always support me emotionally (or with some beers!) thank you Javier, Atalia and Tarek!

To my girlfriend Danahe who would always push me to write this thesis even when there was no motivation due to the COVID lockdown, thank you my love!

At last but not least I would like to thank my parents Victoria and Javier for their endless support, I am who I am thanks to their life lessons and love, this is the reason of why this thesis is dedicated to them. Love you so much!

# Bibliography


Alpher, R. A., & Herman, R. C. (1949). Remarks on the Evolution of the Expanding Universe. *Physical Review*, *75*(7), 1089–1095. doi: 10.1103/PhysRev.75.1089

Bautista, J. (2014). *Baryon acoustic oscillations in the large scale structures of the universe as seen by the sloan digital sky survey* (Doctoral dissertation). Université Paris Diderot. URL: https://tel.archives-ouvertes.fr/tel-01389967

Bennett, C. L., Larson, D., Weiland, J. L., Jarosik, N., Hinshaw, G., Odegard, N., Smith, K. M., Hill, R. S., Gold, B., Halpern, M., Komatsu, E., Nolta, M. R., Page, L., Spergel, D. N., Wollack, E., Dunkley, J., Kogut, A., Limon, M., Meyer, S. S., ... Wright, E. L. (2013). Nine-year Wilkinson Microwave Anisotropy Probe (WMAP) Observations: Final Maps and Results. ApJS, *208*(2). arXiv: 1212.5225 [astro-ph.CO], 20. doi: 10.1088/0067-0049/208/2/20

Blanton, M. R. Et al. (2017). Sloan Digital Sky Survey IV: Mapping the Milky Way, Nearby Galaxies, and the Distant Universe. AJ, *154*(1). arXiv: 1703.00052 [astro-ph.GA], 28. doi: 10.3847/1538-3881/aa7567

Blomqvist, M., du Mas des Bourboux, H., Busca, N. G., de Sainte Agathe, V., Rich, J., Balland, C., Bautista, J. E., Dawson, K., Font-Ribera, A., Guy, J., Le Goff, J.-M., Palanque-Delabrouille, N., Percival, W. J., Pérez-Ràfols, I., Pieri, M. M., Schneider, D. P., Slosar, A., & Yèche, C. (2019). Baryon acoustic oscillations from the cross-correlation of Ly$\alpha$ absorption and quasars in eBOSS DR14. A&A, *629*. arXiv: 1904.03430 [astro-ph.CO], A86. doi: 10.1051/0004-6361/201935641

Colless, M., Dalton, G., Maddox, S., Sutherland, W., Norberg, P., Cole, S., Bland-Hawthorn, J., Bridges, T., Cannon, R., Collins, C., Couch, W., Cross, N., Deeley, K., de Propris, R., Driver, S. P., Efstathiou, G., Ellis, R. S., Frenk, C. S., Glazebrook, K., ... Taylor, K. (2001). The 2dF Galaxy Redshift Survey:

spectra and redshifts. *Monthly Notices of the Royal Astronomical Society*, *328*(4), 1039–1063. doi: 10.1046/j.1365-8711.2001.04902.x

Davis, M., Huchra, J., Latham, D. W., & Tonry, J. (1982). A survey of galaxy redshifts. II. The large scale space distribution. ApJ, *253*, 423–445. doi: 10.1086/159646

Dawson, K. S., Kneib, J.-P., Percival, W. J., Alam, S., Albareti, F. D., Anderson, S. F., Armengaud, E., Aubourg, É., Bailey, S., Bautista, J. E., Berlind, A. A., Bershady, M. A., Beutler, F., Bizyaev, D., Blanton, M. R., Blomqvist, M., Bolton, A. S., Bovy, J., Brandt, W. N., ... Zou, H. (2016). The SDSS-IV Extended Baryon Oscillation Spectroscopic Survey: Overview and Early Data. AJ, *151*(2). arXiv: 1508.04473 [astro-ph.CO], 44. doi: 10.3847/0004-6256/151/2/44

Dawson, K. S., Schlegel, D. J., Ahn, C. P., Anderson, S. F., Aubourg, É., Bailey, S., Barkhouser, R. H., Bautista, J. E., Beifiori, A. r., Berlind, A. A., Bhardwaj, V., Bizyaev, D., Blake, C. H., Blanton, M. R., Blomqvist, M., Bolton, A. S., Borde, A., Bovy, J., Brandt, W. N., ... Zheng, Z. (2013). The Baryon Oscillation Spectroscopic Survey of SDSS-III. AJ, *145*(1). arXiv: 1208.0022 [astro-ph.CO], 10. doi: 10.1088/0004-6256/145/1/10

de Sainte Agathe, V., Balland, C., du Mas des Bourboux, H., Busca, N. G., Blomqvist, M., Guy, J., Rich, J., Font-Ribera, A., Pieri, M. M., Bautista, J. E., Dawson, K., Le Goff, J.-M., de la Macorra, A., Palanque-Delabrouille, N., Percival, W. J., Pérez-Ràfols, I., Schneider, D. P., Slosar, A., & Yèche, C. (2019). Baryon acoustic oscillations at z = 2.34 from the correlations of Ly$\alpha$ absorption in eBOSS DR14. A&A, *629*. arXiv: 1904.03400 [astro-ph.CO], A85. doi: 10.1051/0004-6361/201935638

DESI Collaboration, Aghamousa, A., Aguilar, J., Ahlen, S., Alam, S., Allen, L. E., Allende Prieto, C., Annis, J., Bailey, S., Balland, C., Ballester, O., Baltay, C., Beaufore, L., Bebek, C., Beers, T. C., Bell, E. F., Bernal, J. L., Besuner, R., Beutler, F., ... Zu, Y. (2016a). The DESI Experiment Part I: Science,Targeting, and Survey Design. *arXiv e-prints*. arXiv: 1611.00036 [astro-ph.IM].

DESI Collaboration, Aghamousa, A., Aguilar, J., Ahlen, S., Alam, S., Allen, L. E., Allende Prieto, C., Annis, J., Bailey, S., Balland, C., Ballester, O., Baltay, C., Beaufore, L., Bebek, C., Beers, T. C., Bell, E. F., Bernal, J. L., Besuner, R.,

Beutler, F., ... Zu, Y. (2016b). The DESI Experiment Part II: Instrument Design. *arXiv e-prints*. arXiv: 1611.00037 [astro-ph.IM].

Dey, A., Schlegel, D. J., Lang, D., Blum, R., Burleigh, K., Fan, X., Findlay, J. R., Finkbeiner, D., Herrera, D., Juneau, S., Landriau, M., Levi, M., McGreer, I., Meisner, A., Myers, A. D., Moustakas, J., Nugent, P., Patej, A., Schlafly, E. F., ... Zhou, Z. (2019). Overview of the DESI Legacy Imaging Surveys. AJ, *157*(5), 168. doi: 10.3847/1538-3881/ab089d

Eisenstein, D. J., Annis, J., Gunn, J. E., Szalay, A. S., Connolly, A. J., Nichol, R. C., Bahcall, N. A., Bernardi, M., Burles, S., Castander, F. J., Fukugita, M., Hogg, D. W., Ivezić, Ž., Knapp, G. R., Lupton, R. H., Narayanan, V., Postman, M., Reichart, D. E., Richmond, M., ... Yanny, B. (2001). Spectroscopic Target Selection for the Sloan Digital Sky Survey: The Luminous Red Galaxy Sample. AJ, *122*(5). arXiv: astro-ph/0108153 [astro-ph], 2267–2280. doi: 10.1086/323717

Eisenstein, D. J., Weinberg, D. H. Et al. (2011). SDSS-III: Massive Spectroscopic Surveys of the Distant Universe, the Milky Way, and Extra-Solar Planetary Systems. AJ, *142*(3). arXiv: 1101.1529 [astro-ph.IM], 72. doi: 10.1088/0004-6256/142/3/72

Eisenstein, D. J., Zehavi, I., Hogg, D. W., Scoccimarro, R., Blanton, M. R., Nichol, R. C., Scranton, R., Seo, H.-J., Tegmark, M., Zheng, Z., Anderson, S. F., Annis, J., Bahcall, N., Brinkmann, J., Burles, S., Castand er, F. J., Connolly, A., Csabai, I., Doi, M., ... York, D. G. (2005). Detection of the Baryon Acoustic Peak in the Large-Scale Correlation Function of SDSS Luminous Red Galaxies. ApJ, *633*(2). arXiv: astro-ph/0501171 [astro-ph], 560–574. doi: 10.1086/466512

Geller, M. J., & Huchra, J. P. (1989). Mapping the universe. *Science*, *246*(4932), 897–903. doi: 10.1126/science.246.4932.897

Gontcho A Gontcho, S., Miralda-Escudé, J., & Busca, N. G. (2014). On the effect of the ionizing background on the Ly$\alpha$ forest autocorrelation function. MNRAS, *442*(1). arXiv: 1404.7425 [astro-ph.CO], 187–195. doi: 10.1093/mnras/stu860

Górski, K. M., Hivon, E., Banday, A. J., Wand elt, B. D., Hansen, F. K., Reinecke, M., & Bartelmann, M. (2005). HEALPix: A Framework for High-Resolution Discretization and Fast Analysis of Data Distributed on the Sphere. ApJ, *622*(2). arXiv: astro-ph/0409513 [astro-ph], 759–771. doi: 10.1086/427976

Gunn, J. E., & Peterson, B. A. (1965). On the Density of Neutral Hydrogen in Intergalactic Space. ApJ, *142*, 1633–1636. doi: 10.1086/148444

Laureijs, R., Amiaux, J., Arduini, S., Augueres, J. .-.-L., Brinchmann, J., Cole, R., Cropper, M., Dabin, C., Duvet, L., Ealet, A., Garilli, B., Gondoin, P., Guzzo, L., Hoar, J., Hoekstra, H., Holmes, R., Kitching, T., Maciaszek, T., Mellier, Y., ... Zucca, E. (2011). Euclid Definition Study Report. *arXiv e-prints*. arXiv: 1110.3193 [astro-ph.CO], arXiv:1110.3193.

Liddle, A. (2003). *An introduction to modern cosmology*. Wiley. URL: https://books.google.com.mx/books?vid=9780470848340

Martini, P., Bailey, S., Besuner, R. W., Brooks, D., Doel, P., Edelstein, J., Eisenstein, D., Flaugher, B., Gutierrez, G., Harris, S. E., Honscheid, K., Jelinsky, P., Joyce, R., Kent, S., Levi, M., Prada, F., Poppett, C., Rabinowitz, D., Rockosi, C., ... Wechsler, R. (2018). Overview of the Dark Energy Spectroscopic Instrument. doi: 10.1117/12.2313063

Mo, H., van den Bosch, F., & White, S. (2010). *Galaxy formation and evolution*. Cambridge University Press. URL: https://books.google.com.mx/books?vid=9780521857932

Padmanabhan, N., Schlegel, D. J., Seljak, U., Makarov, A., Bahcall, N. A., Blanton, M. R., Brinkmann, J., Eisenstein, D. J., Finkbeiner, D. P., Gunn, J. E., Hogg, D. W., Ivezić, Ž., Knapp, G. R., Loveday, J., Lupton, R. H., Nichol, R. C., Schneider, D. P., Strauss, M. A., Tegmark, M., & York, D. G. (2007). The clustering of luminous red galaxies in the Sloan Digital Sky Survey imaging data. MNRAS, *378*(3). arXiv: astro-ph/0605302 [astro-ph], 852–872. doi: 10.1111/j.1365-2966.2007.11593.x

Peebles, P. J. E., & Yu, J. T. (1970). Primeval Adiabatic Perturbation in an Expanding Universe. ApJ, *162*, 815. doi: 10.1086/150713

Penzias, A. A., & Wilson, R. W. (1965). A Measurement of Excess Antenna Temperature at 4080 Mc/s. ApJ, *142*, 419–421. doi: 10.1086/148307

Perlmutter, S., Aldering, G., Goldhaber, G., Knop, R. A., Nugent, P., Castro, P. G., Deustua, S., Fabbro, S., Goobar, A., Groom, D. E., Hook, I. M., Kim, A. G., Kim, M. Y., Lee, J. C., Nunes, N. J., Pain, R., Pennypacker, C. R., Quimby, R., Lidman, C., ... Project, T. S. C. (1999). Measurements of $\Omega$ and $\Lambda$ from 42 High-Redshift Supernovae. ApJ, *517*(2). arXiv: astro-ph/9812133 [astro-ph], 565–586. doi: 10.1086/307221

Planck Collaboration, Aghanim, N., Akrami, Y., Ashdown, M., Aumont, J., Baccigalupi, C., Ballardini, M., Banday, A. J., Barreiro, R. B., Bartolo, N., Basak, S., Battye, R., Benabed, K., Bernard, J. .-.-P., Bersanelli, M., Bielewicz, P., Bock, J. J., Bond, J. R., Borrill, J., ... Zonca, A. (2018). Planck 2018 results. VI. Cosmological parameters. *arXiv e-prints*. arXiv: 1807.06209 [astro-ph.CO], arXiv:1807.06209.

Riess, A. G., Filippenko, A. V., Challis, P., Clocchiatti, A., Diercks, A., Garnavich, P. M., Gilliland, R. L., Hogan, C. J., Jha, S., Kirshner, R. P., Leibundgut, B., Phillips, M. M., Reiss, D., Schmidt, B. P., Schommer, R. A., Smith, R. C., Spyromilio, J., Stubbs, C., Suntzeff, N. B., & Tonry, J. (1998). Observational Evidence from Supernovae for an Accelerating Universe and a Cosmological Constant. AJ, *116*(3). arXiv: astro-ph/9805201 [astro-ph], 1009–1038. doi: 10.1086/300499

Ryden, B. (2017). *Introduction to cosmology*. Cambridge University Press. URL: https://books.google.com.mx/books?vid=9781107154834

Seo, H.-J., & Eisenstein, D. J. (2003). Probing Dark Energy with Baryonic Acoustic Oscillations from Future Large Galaxy Redshift Surveys. ApJ, *598*(2). arXiv: astro-ph/0307460 [astro-ph], 720–740. doi: 10.1086/379122

Smoot, G. F. (1999). COBE observations and results (L. Maiani, F. Melchiorri, & N. Vittorio, Eds.). *AIP Conf. Proc.*, *476*(1). arXiv: astro-ph/9902027, 1–10. doi: 10.1063/1.59326

Spergel, D., Gehrels, N., Baltay, C., Bennett, D., Breckinridge, J., Donahue, M., Dressler, A., Gaudi, B. S., Greene, T., Guyon, O., Hirata, C., Kalirai, J., Kasdin, N. J., Macintosh, B., Moos, W., Perlmutter, S., Postman, M., Rauscher, B., Rhodes, J., ... Zhao, F. (2015). Wide-Field InfrarRed Survey Telescope-Astrophysics Focused Telescope Assets WFIRST-AFTA 2015 Report. *arXiv e-prints*. arXiv: 1503.03757 [astro-ph.IM], arXiv:1503.03757.

The Dark Energy Survey Collaboration. (2005). The Dark Energy Survey. *arXiv e-prints*. arXiv: astro-ph/0510346 [astro-ph].

Weinberg, S. (2008). *Gravitation and cosmology: Principles and applications of the general theory of relativity*. Wiley India Pvt. Limited. URL: https://books.google.com.mx/books?vid=9788126517558

Wells, D. C., Greisen, E. W., & Harten, R. H. (1981). FITS - a Flexible Image Transport System. A&AS, *44*, 363.

Wright, E. L., Eisenhardt, P. R. M., Mainzer, A. K., Ressler, M. E., Cutri, R. M., Jarrett, T., Kirkpatrick, J. D., Padgett, D., McMillan, R. S., Skrutskie, M., Stanford, S. A., Cohen, M., Walker, R. G., Mather, J. C., Leisawitz, D., Gautier, I., Thomas N., McLean, I., Benford, D., Lonsdale, C. J., ... Tsai, C.-W. (2010). The Wide-field Infrared Survey Explorer (WISE): Mission Description and Initial On-orbit Performance. AJ, *140*(6). arXiv: 1008.0031 [astro-ph.IM], 1868–1881. doi: 10.1088/0004-6256/140/6/1868

York, D. G. Et al. (2000). The Sloan Digital Sky Survey: Technical Summary. AJ, *120*. arXiv: astro-ph/0006396, 1579–1587. doi: 10.1086/301513

Universidad de Guanajuato

**CAMPUS LEÓN**
**DIVISIÓN DE CIENCIAS E INGENIERÍAS**
**DEPARTAMENTO DE FISICA**

**Asunto**: Revisión de tesis de maestría
León, Gto., Julio de 2020

**DR. DAVID Y. G. DELEPINE**
**DIRECTOR DE LA DIVISIÓN DE CIENCIAS E INGENIERÍAS**
**PRESENTE**

Por este medio le comunico que he revisado la tesis **The Dark Energy Spectroscopic Instrument: Simulations of the first year Lyman-α quasars observations**, escrita por el **Lic. Hiram Kalid Herrera Alcantar**, para efecto de presentarla para la obtención del grado de Maestro en Física.

El texto de la tesis se encuentra completo y se presentan resultados interesantes y bien explicados sobre la construcción de códigos de análisis de la señal de Lyman-alpha dentro de la colaboración internacional DESI. Los resultados y códigos numéricos desarrollados permiten obtener mejores estimaciones de las observaciones y entender la manera en que se verán afectados los valores de las cantidades físicas de interés. Igualmente, he podido ver que el texto fue modificado por el autor para reflejar las sugerencias y comentarios que le fueron expresados durante la revisión. En mi opinión, la tesis cumple con los elementos necesarios para ser defendida ante el comité sinodal asignado en fecha próxima que sea acordada de manera conjunta.

Agradeciendo su amable atención, aprovecho la ocasión para enviarle un cordial saludo.

**ATENTAMENTE**
**“LA VERDAD OS HARÁ LIBRES”**

**DR. LUIS ARTURO UREÑA LÓPEZ**
**PROFESOR TITULAR C**

Loma del Bosque # 103, Col. Loma del Campestre. León, Guanajuato, México. C. P. 37150
Tel: +52 (477) 7885100 Exts. 8420 y 8421, Fax. Ext. 8410.

**Asunto:** Revisión de Tesis de maestría.

León, Gto., a 5 de Agosto del 2020.

**Dr. David Delepine**
**Director de la DCI-UG**
**Campus León.**

Por medio de la presente quiero responder a la solicitud de revisión del trabajo de tesis titulado: ***"The Dark Energy Spectroscopic Instrument: Simulations of the first year Lyman-α quasars observations"***, realizado por Hiram Kalid Herrera Alcantar.

Después de leer el trabajo en cual el objetivo se centra en generar una simulación del espectro de cuásares que DESI observará durante el primer año. Puedo concluir que es un trabajo novedoso y desarrolla resultados que serán importantes para la colaboración DESI.

Por lo mencionado anteriormente creo que el trabajo de tesis es acorde para obtener el grado de maestro en física.

Sin más por el momento

Atentamente

Dr. Oscar Miguel Sabido Moreno.

*C.c.p. Archivo*

UNIVERSIDAD DE GUANAJUATO

León, Gto., 31 de julio del 2020

DR. DAVID DELEPINE
DIVISIÓN DE CIENCIAS E INGENIERÍAS, CAMPUS LEÓN
DIRECTOR

P R E S E N T E

Por medio de la presente, como miembro del jurado calificador designado para revisar el trabajo de grado con título ***"The Dark Energy Spectroscopic Instrument: Simulations of the first year Lyman-α quasars observations"*** que sustenta el ***Lic. Hiram Kalid Herrera Alcantar*** con el fin de obtener el grado de ***Maestría en Física***, hago constar que he leído el trabajo y que avalo el contenido del mismo como un trabajo de Tesis de Maestría.

Sin más por el momento le envío saludos cordiales, quedando de usted para cualquier aclaración.

Atentamente,

Lorena Velázquez I.

Dra. Lorena Velázquez Ibarra

Profesora Asociada C